Identification of fog Particle Size Distribution by a radiative transfer equation inversion

Ali Krayem, Frédéric Bernardin, Arnaud Münch

Identification of fog Particle Size Distribution by a radiative transfer equation inversion

Ali KRAYEM[a,b], Frédéric BERNARDIN[a], Arnaud MÜNCH[b]

[a] *Cerema, ITS research team, 8-10, rue Bernard Palissy, 63017, Clermont-Ferrand, France*
[b] *Université Clermont Auvergne, CNRS, LMBP, F-63000 Clermont-Ferrand, France*

Abstract

We investigate the identification problem of the fog Droplet Size Distribution (DSD) by an inverse method of the 1D radiative transfer equation thanks to spectral radiation measurements in the range 350 nm - 2500 nm. This distribution together with Lorenz-Mie scattering theory allow to compute the optical properties (scattering coefficient, absorption coefficient, and phase function). We prove the well-posedness of the underlying inverse problem then we perform some numerical experiments using synthetic data. The numerical results suggest that the method allows to identify the DSD with different modellings of the radiative transfer (Beer-Lambert, isotropic and anisotropic collision operator).

Keywords:
Optical properties, droplet size distribution, inverse problem, radiative transfer equation, Lorenz-Mie scattering theory, fog.

Contents

Email addresses: ali.krayem@uca.fr (Ali KRAYEM), frederic.bernardin@cerema.fr (Frédéric BERNARDIN), arnaud.munch@uca.fr (Arnaud MÜNCH)

1. Introduction

The World Meteorological Organization defines fog as a suspension of very small, usually microscopic water droplets in the air, reducing visibility at the Earth's surface. Due to the visibility reduction, fog can affect human activities in many fields like free-space optical (FSO) communication, aviation or ground transportation [43, 44, 75]. In this latter field, adverse weather conditions are issues for the development of intelligent vehicle and autonomous driving since perceptive sensors like camera, radar and lidar are largely employed [90, 70, 81, 33, 91, 71]. To evaluate the impact of these adverse conditions on optical sensors, the French research and technical center Cerema operates the European Rain and Fog PAVIN platform (Figure 1) in which optical sensors and cars can be submitted to controlled artificial fog and rain [19, 23, 28, 29]. This platform allows to study human perception in adverse conditions [18, 79], vision system capabilities in fog or rain conditions [13, 65, 73, 57, 62] or computer vision algorithms for object and weather detection [24, 14, 25].

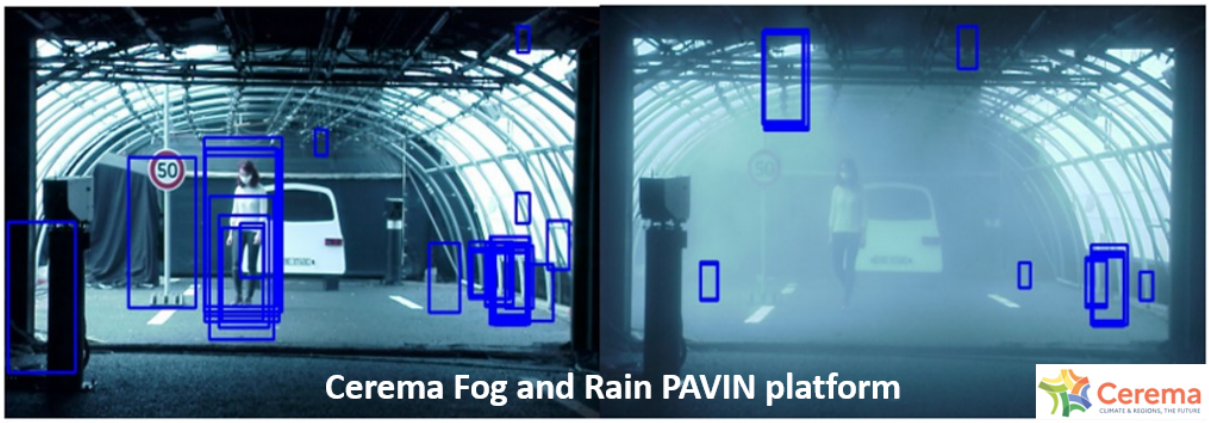

Figure 1: Representation of the evolution of optical sensors at the Cerema's platform in presence of fog.

Many roadmaps [2, 3] of European and worldwide institutions responsible for transportation public policies highlight the driving scenario approach to demonstrate the safety of automated road transport systems, including scenarios based on realistic digital simulation taking into account adverse weather conditions. In order to achieve this objective, ITS research team of Cerema is involved in the Horizon Europe ROADVIEW project (Robust Automated Driving in Extreme Weather) [77] which aims to address the impact of harsh weather on automotive perception sensors and more particularly within the Work Package 3 devoted to the digital simulation. The major issue for the numerical simulation tools use concerns their realism even more so if they are used for autonomous driving security assessment. The simulation of perceptive sensors in fog conditions must take into account the modelling of the propagation of electromagnetic waves through a participating medium. The optical characteristics of this medium must be known in order to simulate the extinction of the radiation. The droplet size distribution for the fog case is a key parameter that governs these optical characteristics depending on the radiation wavelength [10, 41, 29]. The aim of this paper is to propose a method for identifying this distribution from radiation measurements that are interpreted using the radiative transfer equation. We develop a method that allows the identification in a wide range of distributions encountered for natural fogs and artificial ones generated in the PAVIN platform. There is an extensive literature on modeled or measured fog droplet size and other characteristics like liquid water content, total concentration of drops, mean diameter [43, 85, 23, 22, 56, 32, 38, 52, 53, 36, 40, 50, 54, 37, 55, 89, 23, 22, 56, 32, 38, 52, 53, 36, 40, 50, 54, 69, 37, 63, 30, 61]. All the experimental studies show that fog droplet size ranges from a few tenths of a micron to a few tens of microns [74, 39, 43, 47, 44, 66, 16, 76]. Other studies attempt to characterize the droplet size distribution (DSD) by modeling them. Two main categories of laws are used for fitting: shifted gamma laws [26, 83, 64, 88] and log normal laws [83, 12, 22]. In this paper we test our method on DSD obtained by measurement in natural conditions [45], artificial conditions [30] and from models [84].

In a participating medium (fog) containing water particles, the light can be scattered or absorbed. There are numerous models that describe light propagation, such as the radiative transfer equation (RTE), which was introduced in astrophysics, nuclear reactors, and atmospheric science [17, 20, 72]. The radiance is the power per unit area of radiation traveling

or being emitted in a time t at a point $s \in \mathbb{R}^3$, and in a given direction $u \in \mathbb{S}^2$ where $\mathbb{S}^2$ is the unit sphere. The spectral radiance, denoted by L_λ (expressed in $W \cdot m^{-2} \cdot sr^{-1} \cdot m^{-1}$), verifies the following equation [20]:

$$\frac{1}{c}\frac{\partial L_\lambda}{\partial t}(t,s,u) + u.\nabla_s L_\lambda(t,s,u) + \sigma^\lambda_{ext} L_\lambda(t,s,u) = \frac{\sigma^\lambda_{sca}}{4\pi}\int_{\mathbb{S}^2} L_\lambda(t,s,v)\Phi_\lambda(s,v,u)\,dv, \quad (1.1)$$

where c is the light speed in the host medium, $\sigma^\lambda_{ext} = \sigma^\lambda_{sca} + \sigma^\lambda_{abs}$ and σ^λ_{sca} denote the extinction coefficient and the scattering coefficient, respectively, with σ^λ_{abs} the absorbing coefficient at the wavelength λ. The phase function Φ_λ describes the probability that a photon at a point $s \in \mathbb{R}^3$ with directions $v \in \mathbb{S}^2$ undergoes a collision: as a result a photon or a number of photons can appear in the u-directions. The phase function Φ_λ is normalized in the following way:

$$\forall s \in \mathbb{R}^3, \forall u \in \mathbb{S}^2, \frac{1}{4\pi}\int_{\mathbb{S}^2} \Phi_\lambda(s,v,u)\,dv = 1. \quad (1.2)$$

The isotropic case corresponds to a phase function Φ_λ constant equal to one.

We are interested in the reconstruction of the optical properties (scattering coefficient, absorption coefficient and the phase function) in a time-independent case. Concerning the time-dependent case, we mention [5, 42, 78]. To reconstruct these properties, it is necessary to introduce the inverse problem of RTE, which is studied by several authors [67, 68]. Some authors use an exact method to reconstruct these properties [21] based on the knowledge of the Albedo operator, which maps the incoming flux to the outgoing flux under some conditions based on these properties. In [21], they only reconstruct the absorption and scattering coefficients in two dimensions, while in three dimensions they reconstruct all these properties. In dimension $n \geq 3$, Bal and Jollivet [8] investigate the stability of the reconstruction of the scattering and absorption coefficients from the knowledge of the full Albedo operator. There are authors who reconstruct these properties using numerical approximation methods. We mention the work of Klose, Netz, Beuthan, and Hielscher [1] where they evaluated the radiative transfer equation in two dimensions. The authors present a number of tissue phantoms to investigate the sensitivity of the fluence (the integral of radiance) calculated using the radiative transfer equation and comparing it with experimental measurements. In their work, they used the Henyey–Greenstein scattering function (for the phase function). After several tests on various optical properties, the authors observe that without an accurate knowledge of the anisotropy factor of phase function, the measured data cannot be properly predicted. After this study, the authors have introduced the reconstruction of the absorption and scattering coefficients [51] by assuming that the anisotropy factor of the phase function is known.
Egger and Schlottbom [31] identify the scattering and absorption properties by assuming that the phase function is known in three dimensions. These authors use the Tikhonov regularization [59] in Banach spaces to provide a solution to this reconstruction problem.
We also mention [15, 34], where the authors reconstruct the optical properties by assuming that one or two of these properties are known, and by using a reconstruction algorithm based on the Levenberg-Marquardt regularization [60].
Finally, we mention [48, 49, 86, 87, 94], where the authors reconstruct some models of volume

frequency distributions (Rosin–Rammler R-R, Log normal laws L-N, and Normal laws N-N) using Bouguer–Lambert law, $L = L_0 e^{\sigma_{ext}\, d}$, which expresses the attenuation of the luminous flux L_0 at the value of L as a function of the distance d and the extinction coefficient σ_{ext}^{λ}.

The main purpose of this article is to identify the droplet size distribution (DSD) of a fog by radiation measurements. We recall that DSD is the number of water particles per cm^3 for each radius r. The DSD is expressed in $cm^{-3}\mu m^{-1}$ as a function of the radius r of water particles expressed in μm, and is denoted by $N(r)$. The identification of the distribution N allows us to compute the optical properties by using Lorenz-Mie theory [27]. In order to identify the droplet size distribution N, we introduce for all $\varepsilon \geq 0$ the following least-squares problem:

$$\inf_{N \in \mathcal{H}(\mathbb{R}^+)} J_\varepsilon(N) := \frac{1}{2} \sum_{i=1}^{I} \sum_{l=1}^{G} \left(\frac{F_{\lambda_l}(x_i) - M_{\lambda_l}(x_i)}{M_{\lambda_l}(x_i)} \right)^2 + \frac{\varepsilon}{2} \| \sqrt{f} N \|^2_{\mathcal{H}(\mathbb{R}^+)}, \tag{1.3}$$

where

$$\mathcal{H}(\mathbb{R}^+) = \left\{ N \in L^2(\mathbb{R}^+), \int_{\mathbb{R}^+} r^2\, N^2(r) dr < +\infty \right\}$$

endowed with the inner product:

$$(N, \overline{N})_{\mathcal{H}(\mathbb{R}^+)} = \int_{\mathbb{R}^+} r^2\, N(r)\, \overline{N}(r)\, dr.$$

$J_\varepsilon(N)$ is the difference between the measured radiation $M_{\lambda_l}(x_i)$ and the radiation calculated by the radiative transfer equation $F_{\lambda_l}(x_i)$ at point x_i for a wavelength λ_l; I and G represent the number of measurement points and wavelengths, respectively. The ε-term is a regularizing term as it ensures the well-posedness of the problem. Moreover, as a priori knowledge about the droplet size distribution N - almost zero for small radii - that we will identify, we introduce a positive function f in which explodes for small radii.
Figure 2 shows a diagram of the experimental protocol allowing to perform the identification: a spectrally continuous light source (assumed spatially infinite) illuminates a homogeneous foggy medium and spectral measurements are made in forescattering (left) and backscattering (right) situations. For numerical applications, we will consider a Lambertian source.

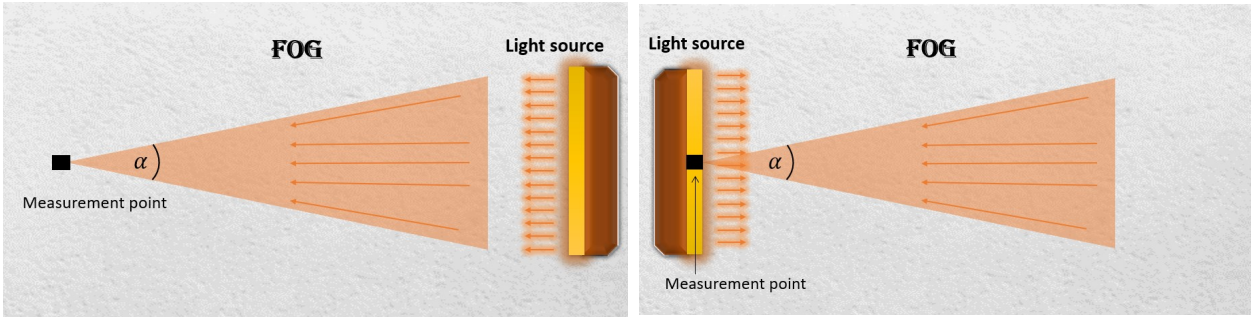

Figure 2: Diagram of the protocol for the measurements.

In this work, we wish to investigate the reconstruction of the DSD with models that may involve a collision operator, and thus not limit ourselves to the basic Beer-Lambert solution.

With some anticipation of the following sections, Figure 3 shows the relative error

$$E_\lambda = \frac{\|L_\lambda - L_{\lambda,0}\|_{L^\infty(X)}}{\|L_\lambda\|_{L^\infty(X)}}$$

between the solution L_λ of the radiative transfer equation with collision (3.4) and the solution $L_{\lambda,0}$ without collision (Beer-Lambert case), with optical parameters given by one of the DSD of Figure 5 (a).

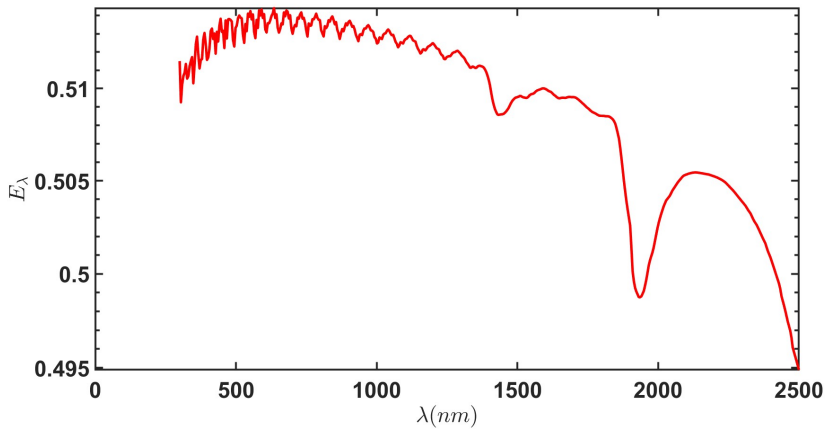

Figure 3: Relative error E_λ between radiance with and without collision operator in function of wavelengths.

We can observe that for different wavelengths between $300\,nm$ and $2500\,nm$, we have an error of 50% between the two radiance which justifies the use of the collision operator. It is therefore needed to develop numerical procedures to solve the complete radiative transfer equation. We then exploit these procedures by using a gradient descent based method to solve our minimization problem: we will introduce an adjoint problem to the RTE allowing to easily calculate the cost function gradient. It is then important to note that the computing time of these procedures depends more on the discretization parameters to solve the integro-differential equation (RTE) and its adjoint problem than the number of parameters describing the DSD: the method we detail in this article doesn't need to model the unknown DSD as that is made in [48, 49, 86, 87, 94].

The paper is organized as follows. In Section 2, we introduce the Lorenz-Mie scattering theory, which enables to express the optical properties with respect to the fog droplet size distributions. We detail in this section the DSD we will use to test the reconstruction method. In Section 3, we recall the existence and uniqueness of the solution of the stationary radiative transfer equation. We also give in this section some explicit solutions to the stationary radiative transfer equation allowing in Section 6 to validate our numerical tools and to study the influence of the numerical parameters used to discretize the RTE. The gradient descent-based inverse problem and the cost function are presented together with their properties in Section 4. We give in this section the expression of the cost function gradient in terms of an adjoint problem to the RTE. In Section 5, we recall Yvon's method [17, 95] to solve the stationary radiative transfer equation and the Barzilai-Borwein algorithm [9] to minimize the cost function J_ε. Numerical results on the DSD identification using synthetic measurements

(output of simulations with real DSDs and some DSDs models as input) in Beer-Lambert modelling case (without multiple scattering), isotropic and anisotropic collision operator cases are presented in Section 7. We end the paper by a conclusion and some perspectives in Section 8.

2. Droplet size distribution, extinction and Mie theory

The World Meteorological Organization (WMO) [93] defines the meteorological visibility as the greatest distance at which a black object of suitable dimensions can be seen and recognized against the horizon sky during daylight or could be seen and recognized during the night if the general illumination were raised to the normal daylight level. Meteorological visibility V_m (expressed in m) is defined by Koschmieder in 1923 as follows [93]:

$$V_m = \frac{3}{\sigma_{ext}} \tag{2.1}$$

where σ_{ext} is the extinction coefficient of the fog for a wavelength of 550 nm (green). We will see in Section 2.1 how to rely this coefficient with the droplet size distribution N of the fog. As mentioned in Section 1, our work is motivated by ITS application and then we will focus on road fogs which are characterized by a meteorological visibility less than 400 meters, that is thanks to (2.1):

$$\sigma_{ext} \geq 7.5 \times 10^{-3}. \tag{2.2}$$

Considering front vehicle lights emitting around 10^3 cd/m^2 and a scotopic human vision (night conditions) detection threshold around 10^{-4} cd/m^2, we will consider fogs with transmittance greater than 10^{-7} or equivalently with optical thickness τ verifying:

$$\tau \leq -\mathrm{Ln}\left(10^{-7}\right) \simeq 16. \tag{2.3}$$

Numerical applications of Section 7 will illustrate our DSD identification method with $\tau = 4$ and DSD we detail in Section 2.2. In the following subsection we present the Mie theory allowing to rely DSD and extinction.

2.1. Lorenz-Mie scattering theory

The Lorenz-Mie theory [27] solves the electromagnetic equations of Maxwell by describing the elastic scattering of an electromagnetic wave by a spherical particle with its diameter and its complex refractive index , $m = n + ik$, with n and k denoting the refractive and absorption indices, respectively. In our work, we use the wavelengths with the Segelstein indices [82]. In light scattering solved by Mie theory, a monochromatic plane wave with wave vector $k = 2\pi/\lambda$ propagates in a medium with refractive index m_1. This incident wave encounters a sphere of radius r. As a result of the interaction, a wave is diffused by the sphere throughout space. Lorenz-Mie theory allows us to compute the scattering properties of a single homogeneous, spherical particle embedded in an homogeneous medium.

The extinction and scattering coefficients are expressed in terms of the droplet size distribution N as follows:

$$\sigma^{\lambda}_{ext}(N) = \int_0^{+\infty} Q^{\lambda}_{ext}(r)\,\pi\,r^2\,N(r)\,dr \quad ; \quad \sigma^{\lambda}_{sca}(N) = \int_0^{+\infty} Q^{\lambda}_{sca}(r)\,\pi\,r^2\,N(r)\,dr. \tag{2.4}$$

Similarly, the phase function can be expressed by the following form:

$$\sigma_{sca}^{\lambda}(N)\,\phi_{\lambda}(\mu,N)=\int_{0}^{+\infty}Q_{sca}^{\lambda}(r)\psi_{\lambda}(r,\mu)\,\pi\,r^{2}\,N(r)\,dr, \tag{2.5}$$

where the scattering and extinction cross sections are given by:

$$Q_{sca}^{\lambda}(r)=\frac{\lambda^{2}}{2\,\pi^{2}\,r^{2}}\sum_{n=1}^{+\infty}(2n+1)\left(|a_{n}(r,\lambda)|^{2}+|b_{n}(r,\lambda)|^{2}\right), \tag{2.6}$$

$$Q_{ext}^{\lambda}(r)=\frac{\lambda^{2}}{2\,\pi^{2}\,r^{2}}\sum_{n=1}^{+\infty}(2n+1)Re\left(a_{n}(r,\lambda)+b_{n}(r,\lambda)\right), \tag{2.7}$$

and ψ_{λ} given by

$$\psi_{\lambda}(r,\mu)=\frac{\lambda^{2}}{2\,\pi^{2}\,r^{2}\,Q_{sca}^{\lambda}(r)}\left(|S_{1}(\mu)|^{2}+|S_{2}(\mu)|^{2}\right). \tag{2.8}$$

S_1 and S_2 are the scattering amplitude functions given by:

$$S_{1}(\mu)=\sum_{n=1}^{+\infty}\frac{2n+1}{n(n+1)}\left(a_{n}(r,\lambda)\pi_{n}(\mu)+b_{n}(r,\lambda)\tau_{n}(\mu)\right), \tag{2.9}$$

$$S_{2}(\mu)=\sum_{n=1}^{+\infty}\frac{2n+1}{n(n+1)}\left(b_{n}(r,\lambda)\pi_{n}(\mu)+a_{n}(r,\lambda)\tau_{n}(\mu)\right), \tag{2.10}$$

where the sequence of polynomials $(\pi_n)_{n\geq 0}$ and $(\tau_n)_{n\geq 0}$ are defined by the recurrences:

$$\begin{cases}\pi_{0}(z)=0,\ \pi_{1}(z)=1,\\ \forall\, n\geq 2\,,\pi_{n}(z)=z\dfrac{2n-1}{n-1}\,\pi_{n-1}(z)-\dfrac{n}{n-1}\,\pi_{n-2}(z),\end{cases}$$

$$\begin{cases}\tau_{0}(z)=0,\ \tau_{1}(z)=z,\\ \forall\, n\geq 2\,,\tau_{n}(z)=z(\tau_{n}(z)-\tau_{n-2}(z))-(2n-1)(1-z^{2})\,\tau_{n-1}(z)+\tau_{n-2}(z).\end{cases}$$

The coefficients a_n and b_n in equations (2.6) and (2.7) are complex numbers called the Lorenz-Mie coefficients, which are composed of the spherical Bessel functions. For more details on a_n and b_n, we refer to [27].
The functions Q_{ext} and Q_{abs} are represented in function of the particle radius r in Figure 4 for different wavelengths (one in the visible $0.55\,\mu m$ and three in infrared $8, 10, 12\,\mu m$).

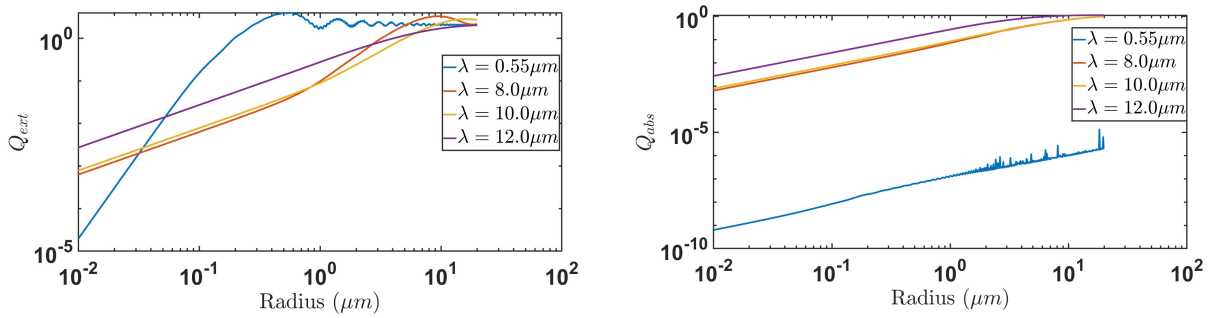

Figure 4: Extinction cross section Q_{ext} (left) and absorption cross section Q_{abs} (right) for four wavelengths in function of particle radius.

The numerical computations of the series introduced above require a truncation. The most commonly used truncation, taking into account the numerical difficulties encountered with Bessel functions, is that of Wiscombe [92]:

$$E(v) = \begin{cases} v + 4v^{1/3} + 1 & \text{if} \quad 0.02 \leq v \leq 8, \\ v + 4.05v^{1/3} + 2 & \text{if} \quad 8 < v \leq 4200, \\ v + 4v^{1/3} + 2 & \text{if} \quad 4200 < v \leq 20000, \end{cases} \tag{2.11}$$

where $E(v)$ is the truncation function of the size parameter $v = 2\pi r/\lambda$.

2.2. Droplet size distributions

We will test our identification method on different fog droplet size distributions, which have been measured in the PAVIN platform or in natural conditions. We will also consider some common DSD models. The measurements were carried out with the PALAS WELAS particle size analyzer [30]. For numerical applications (Section 7), all the DSD are normalized in order to have:

$$\tau \equiv D\sigma_{ext} = 4.0 \text{ (with } D = 1) \Leftrightarrow V_m = 0.75. \tag{2.12}$$

The DSD of artificial fog produced in the PAVIN platform are represented in Figure 5(a). The DSD for a real fog (see Figure 5(b)) were acquired during an episode of fog in the night of March 13 to 14, 2007 on the French Palaiseau site (Paris-Fog campaign [11]).

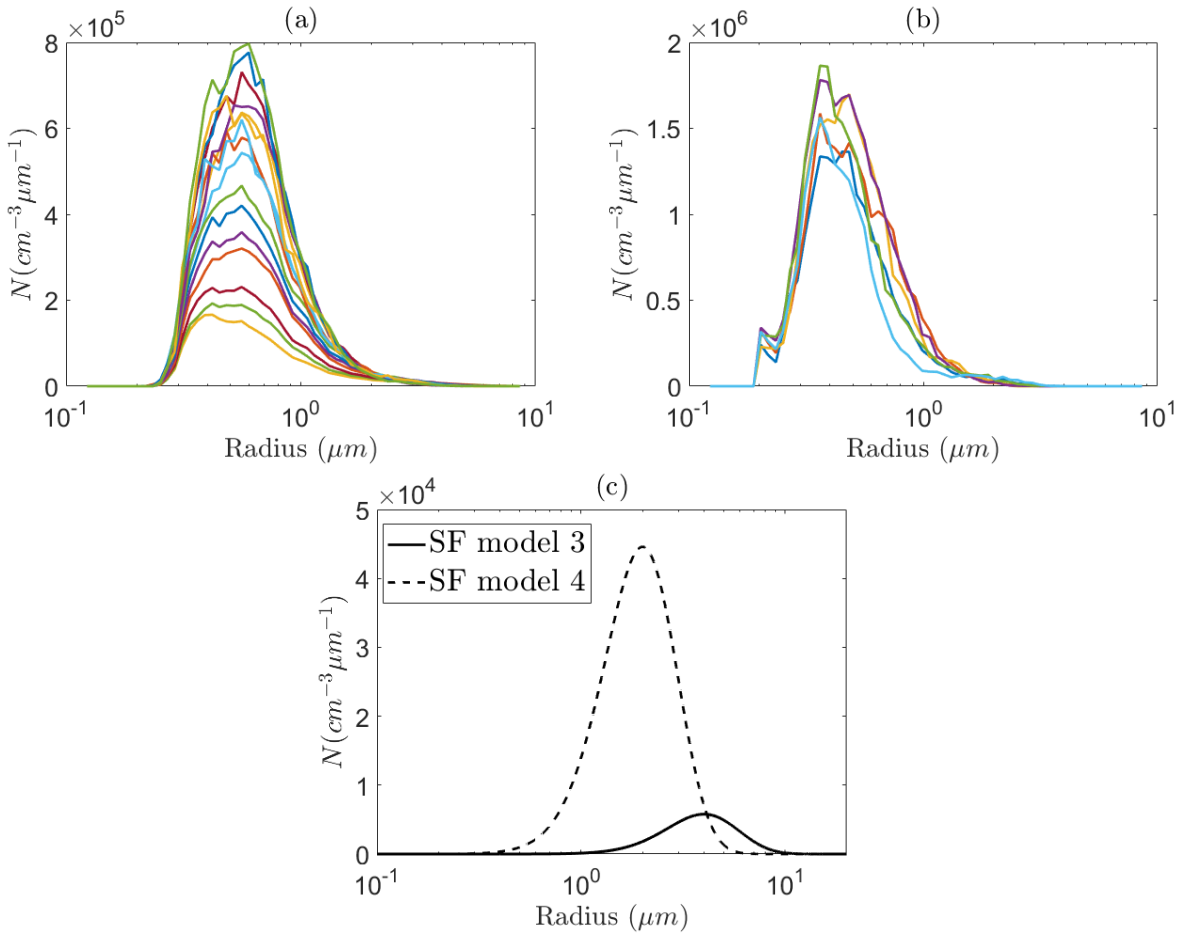

Figure 5: Droplet size distributions N (a) measured at Cerema PAVIN platform, (b) during the Paris-Fog campaign and (c) coming from Shettle and Fenn models.

In order to take into account DSD with bigger droplets, we consider in Figure 5(c) modified Gamma law based models of radiation fogs given by Shettle and Fen [84]):

$$N(r) = c\, r^{\beta} e^{-d r^{\gamma}},\ r \geq 0, \tag{2.13}$$

with the following coefficients:

Model	c	β	d	γ	$r_m(\mu m)$
3	428.15	6	1.5	1	4
4	211317	6	3.0	1	2

Table 1: Coefficients given in [84] for modified Gamma laws (2.13).

where r_m represents the peak position for each model.

3. One-dimensional stationary radiative transfer equation

We are interested in the stationary radiative transfer equation in one-dimensional space (stationary linear Boltzmann equation): for a wavelength λ,

$$\mu\frac{\partial \tilde{L}_\lambda}{\partial x}(x,\mu,N)+\sigma_{ext}^\lambda(N)\tilde{L}_\lambda(x,\mu,N)=\mathcal{K}\tilde{L}_\lambda(x,\mu,N)+q_\lambda(x,\mu),\ (x,\mu)\in[0,+\infty)\times[-1,1] \tag{3.1}$$

with the following boundary conditions:

$$\tilde{L}(0,\mu,N)=L^+(\mu)\quad\text{for}\quad\mu>0\quad;\quad\lim_{x\to+\infty}\tilde{L}(x,\mu,N)=0\quad\text{for}\quad\mu<0, \tag{3.2}$$

where $\mu=\cos(\theta)$ denotes the cosine of the propagation angle, $N\in L^2(\mathbb{R}^+)$ is the droplet size distribution, and

$$\begin{cases}\sigma_{ext}^\lambda(N)=\sigma_{abs}^\lambda(N)+\sigma_{sca}^\lambda(N),\\ \mathcal{K}L_\lambda(x,\mu,N)=\dfrac{\sigma_{sca}^\lambda(N)}{2}\displaystyle\int_{-1}^{1}\Phi_\lambda(\mu,\mu',N)\,L_\lambda(x,\mu',N)\,d\mu',\\ \forall\,(\mu,\mu')\in[-1,1]^2,\ \Phi_\lambda(\mu,\mu',N)=\dfrac{1}{2\pi}\displaystyle\int_0^{2\pi}\phi_\lambda(\mu\mu'+\sqrt{1-\mu^2}\sqrt{1-\mu'^2}\cos(\omega),N)\,d\omega.\end{cases} \tag{3.3}$$

The condition (1.2) in one-dimensional space becomes

$$\forall\,\mu\in[-1,1],\quad\frac{1}{2}\int_{-1}^{1}\Phi_\lambda(\mu,\mu',N)\,d\mu'=1.$$

According to the results of Case-Zweifel [17] and Dautray-Lions [80], the problem (3.1)-(3.2) has a unique solution which decreases exponentially towards 0 as x tends to infinity. In the squel, we will restrict the space domain to $[0,D]$ and the radiative transfer equation (3.1) posed in $[0,D]$ is given by the following problem [6, 7]:

$$\begin{cases}\mu\dfrac{\partial L_\lambda}{\partial x}(x,\mu,N)+\sigma_{ext}^\lambda(N)L_\lambda(x,\mu,N)=\mathcal{K}L_\lambda(x,\mu,N)+q_\lambda(x,\mu),\ (x,\mu)\in X\\ L_\lambda(0,\mu,N)=L_\lambda^+(\mu)\quad\text{for}\quad\mu>0\quad\text{and}\quad L_\lambda(D,\mu,N)=L_\lambda^-(\mu)\quad\text{for}\quad\mu<0,\end{cases} \tag{3.4}$$

where $X=[0,D]\times([-1,0)\cup(0,1])$. L_λ^- is the spectral radiance value at $x=D$ which is small if D is large enough. For the numerical applications, we will use $L_\lambda^-=0$.

3.1. Existence and uniqueness of the solution of stationary radiative transfer equation

In this section, we review the existence and uniqueness of the solution of stationary radiative transfer equation (3.4).

Theorem 3.1. *[7] Assume $\sigma_{abs}^\lambda(N)>0$ and suppose that $\dfrac{\sigma_{sca}^\lambda(N)}{2}\Phi_\lambda\in C_b(([-1,0)\cup(0,1])^2\times\mathbb{R}^+)$ and*

$$q_\lambda\in L^\infty(X)\quad,\quad L_\lambda^+\in L^\infty((0,1]),L_\lambda^-\in L^\infty([-1,0)),$$

where C_b is the space of bounded continuous functions. The problem (3.4) has a unique solution in $C_b(X)$ which satisfies the following estimate

$$\|L_\lambda\|_{L^\infty(X)}\le\max\left(\|L_\lambda^-\|_{L^\infty([-1,0))},\|L_\lambda^+\|_{L^\infty((0,1])},\frac{1}{\sigma_{abs}^\lambda(N)}\|q_\lambda\|_{L^\infty(X)}\right). \tag{3.5}$$

3.2. Some explicit solutions of the stationary radiative transfer equation

In some cases, we provide exact solutions for the stationary radiative transfer equation used in the sequel to check our numerical approximations.

3.2.1. Case without collision operator ($\mathcal{K}L_\lambda \equiv 0$) and $q_\lambda \equiv 0$

We are interested in the following system, with $\sigma^\lambda_{ext}(N) > 0$:

$$\begin{cases} \mu \dfrac{\partial L_\lambda}{\partial x}(x,\mu) + \sigma^\lambda_{ext}(N) L_\lambda(x,\mu) = 0, \ (x,\mu) \in X \\ L_\lambda(0,\mu) = L^+_\lambda(\mu), \ \mu > 0 \quad \text{and} \quad L_\lambda(D,\mu) = 0, \mu < 0. \end{cases} \tag{3.6}$$

It is easy to show the solution of (3.6) is:

$$L_\lambda(x,\mu) = L^+_\lambda(\mu)\, e^{-\sigma^\lambda_{ext}(N)\dfrac{x}{\mu}} \mathbb{1}_{\mu>0}. \tag{3.7}$$

3.2.2. Case with a source expressed by a Dirac measure

We are interested in the following system, with $\sigma^\lambda_{ext}(N) > 0$ and $0 < c < D$ real numbers:

$$\begin{cases} \mu \dfrac{\partial L_\lambda}{\partial x}(x,\mu) + \sigma^\lambda_{ext}(N) L_\lambda(x,\mu) = f(\mu)\delta_c(x), \ (x,\mu) \in X \\ L_\lambda(0,\mu) = 0, \ \mu > 0 \quad \text{and} \quad L_\lambda(D,\mu) = 0, \ \mu < 0. \end{cases} \tag{3.8}$$

The solution of (3.8) is :

$$L_\lambda(x,\mu) = \frac{f(\mu)}{|\mu|} e^{-\sigma^\lambda_{ext}(N)\dfrac{(x-c)}{\mu}} \mathbb{1}_{(x-c)\mu>0}. \tag{3.9}$$

3.2.3. Case with phase function $\Phi_\lambda \equiv 1$ and source term q_λ expressed by the Dirac measure

We are interested in the problem discussed in paragraph 4 of [80] with $0 < c < 1$:

$$\begin{cases} \mu \dfrac{\partial L_\lambda}{\partial x}(x,\mu) + L_\lambda(x,\mu) = \dfrac{c}{2}\displaystyle\int_{-1}^{1} L_\lambda(x,\mu')d\mu' + \frac{1}{2}\delta(x), \ x \in \mathbb{R}, \ \mu \in [-1,0) \cup (0,1], \\ L_\lambda(-\infty,\mu) = 0, \ \mu > 0 \quad ; \quad L_\lambda(+\infty,\mu) = 0, \ \mu < 0. \end{cases} \tag{3.10}$$

The solution is expressed by applying the Fourier transform to the variable μ, and by using Cauchy's theorem of complex analysis.

The expression of $T(x) := \displaystyle\int_{-1}^{1} L(x,\mu)\, d\mu$, according to [80] is:

$$\forall\, x > 0, \ T(x) = \frac{\xi_0}{c}\frac{1-\xi_0^2}{\xi_0^2 + c - 1}\, e^{-\xi_0 x} + \int_1^{+\infty} \frac{e^{-tx}}{2t\left[\left(1 - \frac{c}{2t}\log\frac{t+1}{t-1}\right)^2 + \left(\frac{c\pi}{2t}\right)^2\right]}\, dt, \tag{3.11}$$

where $0 < \xi_0 \leq 1$ verifies $i\xi_0 - c\,\mathrm{atan}(i\xi_0) = 0$. We give in table 2 some values of ξ_0 according to c.

c	0.25	0.5	0.75	0.9
ξ_0	9.993×10^{-1}	9.575×10^{-1}	$7.755\times\ 10^{-1}$	5.254×10^{-1}

Table 2: Approximation of ξ_0 for several values of c.

4. Identification of the DSD by a least-squares optimization method

In this section, we present the inverse problem for identifying the droplet size distribution N from radiation measurements.

4.1. The cost function and the minimization problem

The measurements at wavelength λ_l, at a point x_i of the x-axis is determined by:

$$M_l^i \equiv M_{\lambda_l}(x_i) = \int_a^b L^\star_{\lambda_l}(x_i, \mu)\, d\mu\,, \quad \forall\, 1 \le i \le I,\ 1 \le l \le G, \tag{4.1}$$

where I and G represent the numbers of measurement points and wavelengths, respectively. The two parameters a and b are defined as follows:

$$a = \cos\left(\theta' + \frac{\alpha}{2}\right) \qquad ; \qquad b = \cos(\theta') \tag{4.2}$$

where α designates the aperture angle of the sensor, and θ' is the position angle of the sensor relative to the source ($\theta' = 0°$ for forescattering measurements, and $\theta' = 180°$ for backscattering measurements).
$L^\star_\lambda(x, \mu)$ is the "real" spectral radiance in the direction μ, at point x and for the wavelength λ. For the numerical applications, we will use synthetic measurements obtained by (7.1) and by:

$$L^\star_\lambda(x, \mu) = L_\lambda(x, \mu, N^\star), \tag{4.3}$$

that is $L^\star_\lambda$ is the solution of the stationary radiative transfer equation (3.4) with a known droplet size distribution $N^\star$ measured in the PAVIN platform, in natural foggy conditions or coming from DSD modelling recalled in the Introduction and detailed in Section 6.
In order to identify the droplet size distribution N, we introduce for all $\varepsilon \ge 0$ the following least-squares problem:

$$\inf_{N \in \mathcal{H}(\mathbb{R}^+)} J_\varepsilon(N), \tag{4.4}$$

where

$$J_\varepsilon(N) = J_1(N) + \frac{\varepsilon}{2}\, \|\sqrt{f}\, N\|^2_{\mathcal{H}(\mathbb{R}^+)}, \tag{4.5}$$

and

$$J_1(N) = \frac{1}{2} \sum_{i=1}^{I} \sum_{l=1}^{G} \left(\frac{\displaystyle\int_a^b L_{\lambda_l}(x_i, \mu)\, d\mu - M_{\lambda_l}(x_i)}{M_{\lambda_l}(x_i)} \right)^2 . \tag{4.6}$$

The cost function defined in (4.5) represents the difference between the synthetic measurements and the model output, including the regularity term.

Theorem 4.1. *For all $\varepsilon \ge 0$, the least squares problem (4.4)-(4.5) admits a unique solution in $\mathcal{H}(\mathbb{R}^+)$.*

Proof. It is easy to check that the cost function J_ε defined in (4.5) is continuous, differentiable, and strictly convex. Then our problem admits a unique minimum.

4.2. The cost function gradient and the adjoint problem

Here we show the differentiability of the cost function and express its gradient thanks to the adjoint problem associated to the radiative transfer equation.

Proposition 4.1. *For all $\varepsilon \geq 0$, the function J_ε is differentiable and the directional derivative is as follows:*

$$DJ_\varepsilon(N)\cdot \overline{N} = (\nabla J_\varepsilon(N), \overline{N})_{\mathcal{H}(\mathbb{R}^+)} = \int_0^{+\infty} r^2\ (\nabla J_\varepsilon(N))(\,r)\,\overline{N}(r)\,dr,$$

where

$$\nabla J_\varepsilon(N) = -\pi \sum_{l=1}^{G} \left[Q_{ext}^{\lambda_l} W_{\lambda_l}(N)\right] + \frac{\pi}{2}\sum_{l=1}^{G}\left[Q_{sca}^{\lambda_l} R_{\lambda_l}(N)\right] + \varepsilon f N, \tag{4.7}$$

with for all wavelengths λ,

$$W_\lambda(N) = \int_{-1}^{1}\int_0^D p_\lambda(x,\mu,N)\,L_\lambda(x,\mu,N)\,dx\,d\mu, \tag{4.8}$$

$$R_\lambda(N) = \frac{1}{2\pi}\int_{\mu=-1}^{1}\int_0^D p_\lambda(x,\mu,N)\left(\int_{\mu'=-1}^{1} L_\lambda(x,\mu',N)\left(\int_0^{2\pi}\psi_\lambda(r,\mu_0)d\omega\right)d\mu'\right)dx\,d\mu.$$

L_λ verifies (3.4), and p_λ verifies the adjoint problem defined by

$$\begin{cases} -\mu\,\dfrac{\partial p_\lambda}{\partial x}(x,\mu,N) + \sigma_{ext}^{\lambda}(N)\,p_\lambda(x,\mu,N) = \mathcal{K}p_\lambda(x,\mu,N) + q_\lambda(x,\mu,N),\ (x,\mu)\in X \\ \\ p_\lambda(0,\mu,N) = 0,\ \mu<0 \quad \textit{and} \quad p_\lambda(D,\mu,N) = 0,\ \mu>0, \end{cases} \tag{4.9}$$

with

$$q_\lambda(x,\mu,N) = \sum_{i=1}^{I}\left(\frac{\displaystyle\int_a^b L_\lambda(x_i,\mu,N)\,d\mu - M_\lambda(x_i)}{(M_{\lambda_l}(x_i))^2}\right)\mathbb{1}_{(a,b)}(\mu)\,\delta_{x_i}(x). \tag{4.10}$$

Proof. The directional derivative of the cost function (4.5) according to $\overline{N}$ is given by the following form (see Appendix A):

$$\begin{aligned} DJ_\varepsilon(N)\cdot\overline{N} = &-\sum_{l=1}^{G}\left[\sigma_{ext}^{\lambda_l}(\overline{N})\int_{-1}^{1}\int_0^D p_{\lambda_l}(x,\mu,N)\,L_{\lambda_l}(x,\mu,N)\,dx\,d\mu\right] \\ &+\frac{1}{2}\sum_{l=1}^{G}\left[\sigma_{sca}^{\lambda_l}(\overline{N})\int_{\mu=-1}^{1}\int_0^D p_{\lambda_l}(x,\mu,N)\left(\int_{\mu'=-1}^{1} L_{\lambda_l}(x,\mu',N)\Phi_{\lambda_l}\left(\mu,\mu',\overline{N}\right)d\mu'\right)dxd\mu\right] \\ &+\varepsilon\int_0^{+\infty} r^2\,f(r)\,N(r)\,\overline{N}(r)\,dr. \end{aligned} \tag{4.11}$$

Moreover,

$$\sigma_{sca}^{\lambda_l}(\overline{N})\,\Phi_\lambda(\mu,\mu',\overline{N}) = \frac{1}{2\pi}\int_0^{2\pi} \sigma_{sca}^{\lambda_l}(\overline{N})\,\phi_\lambda(\mu\mu' + \sqrt{1-\mu^2}\sqrt{1-\mu'^2}\cos(\omega),\overline{N})\,d\omega, \quad (4.12)$$

by (2.5), and noting that $\mu_0 = \mu\mu' + \sqrt{1-\mu^2}\sqrt{1-\mu'^2}\cos(\omega)$, we have

$$\sigma_{sca}^{\lambda}\,\phi_\lambda(\mu_0,\overline{N}) = \int_0^{+\infty} Q_{sca}^{\lambda}(r)\psi_\lambda(r,\mu_0)\,\pi\,r^2\,\overline{N}(r)\,dr, \quad (4.13)$$

then

$$\sigma_{sca}^{\lambda_l}(\overline{N})\,\Phi_\lambda(\mu,\mu',\overline{N}) = \frac{1}{2\pi}\int_0^{2\pi}\int_0^{+\infty} Q_{sca}^{\lambda}(r)\psi_\lambda(r,\mu_0)\,\pi\,r^2\,\overline{N}(r)\,dr\,d\omega, \quad (4.14)$$

where ψ_λ is defined in (2.8).
By injecting (2.4) and (4.14) in (4.11), we get

$$\begin{aligned} DJ_\varepsilon(N)\cdot\overline{N} = &-\pi\sum_{l=1}^{G}\left[\int_0^{+\infty} Q_{ext}^{\lambda_l}(r)\,E_{\lambda_l}(N)\,r^2\,\overline{N}(r)\,dr\right] \\ &+\frac{\pi}{2}\sum_{l=1}^{G}\left[\int_0^{+\infty} Q_{sca}^{\lambda_l}(r)\,R_{\lambda_l}(N)r^2\,\overline{N}(r)\,dr\right] + \varepsilon\int_0^{+\infty} r^2\,f(r)\,N(r)\,\overline{N}(r)\,dr, \end{aligned} \quad (4.15)$$

then, we obtain the formula (4.7).

5. Numerical schemes to approximate the RTE and its adjoint problem

In this section, we present the approximation of one-dimensional stationary radiative transfer equation by using Yvon's method [95]. In order to use this method, we need to decompose the phase function on the Legendre polynomials basis. In the following, we give the minimization algorithm to minimize the cost function J_ε.

5.1. Decomposition of the phase function on Legendre basis

In this part, we present the decomposition of the phase function Φ_λ on Legendre polynomials basis [35]. We recall that the Legendre polynomials are defined for all $\mu \in [-1,1]$ by the following recurrence (see [58]):

$$\begin{cases} P_0(\mu) = 1 \quad , \quad P_1(\mu) = \mu, \\ \forall\, n \geq 1,\ P_{n+1}(\mu) = \dfrac{(2n+1)}{(n+1)}\,\mu\,P_n(\mu) - \dfrac{n}{(n+1)}\,P_{n-1}(\mu). \end{cases} \quad (5.1)$$

Lemma 5.1. *The phase function Φ_λ defined in (3.1) can be decomposed as follows:*

$$\forall\,(\mu,\mu') \in [-1,1]^2,\ \forall\, N \in L^2(\mathbb{R}^+),\ \Phi_\lambda(\mu,\mu',N) = \sum_{k=0}^{+\infty} A_{\lambda,k}(N)\,P_k(\mu)\,P_k(\mu'), \quad (5.2)$$

with

$$A_{\lambda,k}(N) = \frac{1}{\sigma^{\lambda}_{sca}(N)} \int_0^{+\infty} Q^{\lambda}_{sca}(r) \tilde{A}_{\lambda,k}(r)\, \pi\, r^2\, N(r)\, dr, \tag{5.3}$$

and

$$\forall\, r > 0,\ \tilde{A}_{\lambda,k}(r) = \frac{\lambda^2(2k+1)}{4\,\pi^2\, r^2\, Q^{\lambda}_{sca}(r)} \sum_{i=0}^{+\infty} \sum_{j=0}^{+\infty} (\alpha_i\, \overline{\alpha}_j + \beta_i\, \overline{\beta}_j) \int_{-1}^{1} P_i(\mu)\, P_j(\mu)\, P_k(\mu)\, d\mu, \tag{5.4}$$

where $\alpha,\ \beta \in \mathbb{C}$ are determined in Appendix B. $\overline{\alpha}, \overline{\beta}$ are the complex conjugates of α, β and we have [4]:

$$\int_{-1}^{1} P_i(\mu)\, P_j(\mu)\, P_k(\mu)\, d\mu = \begin{cases} 0 \ \textit{if } i+j<k \ \textit{ or } j+k<i \ \textit{ or } i+j+k \ \textit{ is odd} \\ 2\dfrac{(2s-2i)(2s-2k)(2s-2j)}{(2s-1)!} \left[\dfrac{s!}{(s-i)!(s-j)!(s-k)!}\right] \quad \textit{else,} \end{cases}$$

with $s = (i+j+k)/2$.

Proof. Let us assume that the functions S_1 and S_2 defined in (2.9)-(2.10) are decomposed on the Legendre basis $(P_k)_{k\geq 0}$ as follows:

$$\forall\, \mu \in [-1,1],\ S_1(\mu) = \sum_{i=0}^{+\infty} \alpha_i\, P_i(\mu) \quad ; \quad S_2(\mu) = \sum_{i=0}^{+\infty} \beta_i\, P_i(\mu). \tag{5.5}$$

From (2.8), we deduce that

$$\begin{aligned} \psi_{\lambda}(r,\mu) =& \frac{\lambda^2}{2\,\pi^2\, r^2\, Q^{\lambda}_{sca}(r)} \sum_{i=0}^{+\infty} \sum_{j=0}^{+\infty} (\alpha_i\, \overline{\alpha}_j + \beta_i\, \overline{\beta}_j) \int_{-1}^{1} P_i(\mu)\, P_j(\mu)\, d\mu \\ =& \sum_{k=0}^{+\infty} \tilde{A}_{\lambda,k}(r)\, P_k(\mu) \end{aligned} \tag{5.6}$$

Moreover,

$$\begin{aligned} \phi_{\lambda}(\mu,N) =& \frac{1}{\sigma^{\lambda}_{sca}(N)} \int_0^{+\infty} Q^{\lambda}_{sca}(r) \psi_{\lambda}(r,\mu)\, \pi\, r^2\, N(r)\, dr \\ =& \frac{1}{\sigma^{\lambda}_{sca}(N)} \int_0^{+\infty} Q^{\lambda}_{sca}(r) \left(\sum_{k=0}^{+\infty} \tilde{A}_{\lambda,k}(r)\, P_k(\mu) \right) \pi\, r^2\, N(r)\, dr \\ =& \sum_{k=0}^{+\infty} A_{\lambda,k}(N)\, P_k(\mu), \end{aligned} \tag{5.7}$$

where

$$A_{\lambda,k}(N) = \frac{1}{\sigma^{\lambda}_{sca}(N)} \int_0^{+\infty} Q^{\lambda}_{sca}(r) \tilde{A}_{\lambda,k}(r)\, \pi\, r^2\, N(r)\, dr. \tag{5.8}$$

Then,

$$\begin{aligned}\Phi_\lambda(\mu,\mu',N) &= \frac{1}{2\pi}\int_0^{2\pi}\phi_\lambda(\mu\mu'+\sqrt{1-\mu^2}\sqrt{1-\mu'^2}\cos(\omega),N)\,d\omega \\ &= \frac{1}{2\pi}\sum_{k=0}^{+\infty}A_{\lambda,k}(N)\int_0^{2\pi}P_k(\mu\mu'+\sqrt{1-\mu^2}\sqrt{1-\mu'^2}\cos(\omega))d\omega,\end{aligned} \tag{5.9}$$

using Legendre's polynomial addition theorem [58]: for all $n \geq 1$,

$$\begin{aligned}\forall\,(\mu,\mu')\in[-1,1]^2,\forall w\in[0,2\pi],\,&P_n\left(\mu\mu'+\sqrt{1-\mu^2}\sqrt{1-\mu'^2}\cos w\right) \\ &= P_n(\mu)P_n\left(\mu'\right)+2\sum_{m=1}^{n}\frac{(n-m)!}{(n+m)!}P_n^m(\mu)P_n^m\left(\mu'\right)\cos(mw),\end{aligned}$$

which results in

$$\forall\,(\mu,\mu')\in[-1,1]^2,\frac{1}{2\,\pi}\int_0^{2\pi}P_n\left(\mu\mu'+\sqrt{1-\mu^2}\sqrt{1-\mu'^2}\cos w\right)dw = P_n(\mu)P_n\left(\mu'\right).$$

Then, from (5.9) and Legendre's polynomial addition theorem, we obtain:

$$\Phi_\lambda(\mu,\mu',N)=\sum_{k=0}^{+\infty}A_{\lambda,k}(N)\,P_k(\mu)\,P_k(\mu').$$

5.2. Approximation of the stationary radiative transfer equation using Yvon's method

To solve the stationary radiative transfer equation, we use Yvon's method [95] which is a decomposition method based on the double basis of Legendre polynomials $(P_n(2\cdot-1))_{n\geq0}$ for $\mu\in[-1,0)$ and $(P_n(2\cdot+1))_{n\geq0}$ for $\mu\in(0,1]$. Yvon's method begins by splitting the L_λ into two functions, one ℓ_λ^+ corresponds to photons having a $\mu>0$, the other ℓ_λ^- corresponds to photons having a $\mu<0$, and consider each of these parts as a separate function.
The radiance L_λ, for K Legendre polynomials, is decomposed as follows [95]:

$$L_\lambda(x,\mu)=\begin{cases}\displaystyle\sum_{j=0}^{K}(2j+1)\ell_{\lambda,j}^-(x,N)P_j(2\mu+1) & \text{if} \quad \mu<0\\ \displaystyle\sum_{j=0}^{K}(2j+1)\ell_{\lambda,j}^+(x,N)P_j(2\mu-1) & \text{if} \quad \mu>0,\end{cases} \tag{5.10}$$

and suppose that the source term q_λ in (3.1) is decomposed as follows:

$$q_\lambda(x,\mu)=\sum_{i=0}^{K}q_{\lambda,i}(x)\,P_i(\mu). \tag{5.11}$$

By injecting (5.9), (5.10), and (5.11) into (3.1), we get two systems of size $K+1$ that verify the functions $\ell^+_{\lambda,j}$, $\ell^-_{\lambda,j}$ [95]:

$$\begin{cases} \frac{1}{2}\frac{j}{2j+1}\frac{d\ell^+_{\lambda,j-1}}{dx}(x,N) + \frac{1}{2}\frac{j+1}{2j+1}\frac{d\ell^+_{\lambda,j+1}}{dx}(x,N) + \frac{1}{2}\frac{d\ell^+_j}{dx}(x,N) + \sigma^\lambda_{ext}(N)\ell^+_j(x,N) \\ = \frac{1}{2}\sigma^\lambda_{sca}(N)\sum_{n=0}^{K}(2n+1)\left(\Gamma^{\alpha,\beta}_{j,n}\ell^-_{\lambda,n}(x,N) + \Gamma^{\alpha,\alpha}_{j,n}\ell^+_n(x,N)\right) + \sum_{n=0}^{K} q_{\lambda,n}(x)\alpha_{n,j}, 0 \le j \le K \\ -\frac{1}{2}\frac{j}{2j+1}\frac{d\overline{\ell}^-_{\lambda,j-1}}{dx}(x,N) - \frac{1}{2}\frac{j+1}{2j+1}\frac{d\overline{\ell}^-_{\lambda,j+1}}{dx}(x,N) - \frac{1}{2}\frac{d\ell^-_j}{dx}(x,N) + \sigma^\lambda_{ext}(N)\overline{\ell}^-_{\lambda,j}(x) \\ = \frac{1}{2}\sigma^\lambda_{sca}(N)\sum_{n=0}^{K}(2n+1)\left(\Gamma^{\beta,\beta}_{j,n}\overline{\ell}^-_{\lambda,n}(x,N) + \Gamma^{\beta,\alpha}_{j,n}\overline{\ell}^+_{\lambda,n}(x,N)\right) + \sum_{n=0}^{K} q_{\lambda,n}(D-x)\beta_{n,j}, 0 \le j \le K \\ \forall x \in [0,D], \left(\ell^-_{\lambda,K+1}\right)'(x,N) = \left(\ell^+_{\lambda,K+1}\right)'(x,N) = 0, \\ \left(\ell^+_{\lambda,j}(0,N)\right))_{0\le j\le K} \text{ and } \left(\ell^-_{\lambda,j}(D,N)\right)_{0\le j\le K} \text{ given,} \end{cases} \tag{5.12}$$

where we put $\overline{\ell}^\pm_{\lambda,k}(\cdot,N) = \ell^\pm_{\lambda,k}(D-\cdot,N)$, and

$$\forall j \ge 0, \forall n \ge 0, \Gamma^{u,v}_{\lambda,j,n} \equiv \Gamma^{u,v}_{\lambda,j,n}(N) = \sum_{k=0}^{K} A_{\lambda,k}(N)\, u_{k,j}\, v_{k,n},$$

for any real families $(u_{p,q})_{p\ge0,q\ge0}$, $(v_{p,q})_{p\ge0,q\ge0}$ while $A_{\lambda,k}$ is defined in (5.3), and

$$\forall k \ge 0, \forall n \ge k, \alpha_{n,k} = \int_0^1 P_n(\mu)P_k(2\mu-1)d\mu \quad ; \quad \beta_{n,k} = \int_{-1}^0 P_n(\mu)P_k(2\mu+1)d\mu. \tag{5.13}$$

Eventually, our system (5.12) reads in a compact form as follows:

$$\begin{cases} A\, L'_\lambda(x) + B\, L_\lambda(x) = C_1\, L_\lambda(x) + C_2\, L_\lambda(D-x) + E(x), 0 < x < D, \\ L_\lambda(0) \text{ given,} \end{cases} \tag{5.14}$$

with A, B, C_1 and C_2 some matrices of size $(2K+2)\times(2K+2)$, A tridiagonal and B diagonal, E a vector of size $2K+2$.
In order to solve (5.14), we use the so-called "source iteration method" [see 7, chapter 5 section 2] combined with the implicit Euler scheme.
To use the same discretization for the adjoint problem (4.9), we make a change of variable of $\tilde{x} = D - x$ to obtain a problem similar to the radiative transfer equation. Then, we obtain

$$p_\lambda(x,\mu) = \begin{cases} \sum_{k=0}^{K}(2\,k+1)\, d^-_{\lambda,k}(x,N)P_k(2\,\mu+1) \quad \text{if} \quad \mu < 0, \\ \sum_{k=0}^{K}(2\,k+1)\, d^+_{\lambda,k}(x,N)P_k(2\,\mu-1) \quad \text{if} \quad \mu > 0. \end{cases} \tag{5.15}$$

5.3. Approximation of the gradient

By injecting (5.10) and (5.15) into (4.7), and by using the trapezoidal rule for the integral in x, the gradient for K Legendre polynomials is given as follows:

$$\nabla J_\varepsilon(N) \approx -\pi \sum_{l=1}^{G} Q_{ext}^{\lambda_l} W_{\lambda_l}(N) + \frac{\pi}{2} \sum_{l=1}^{G} Q_{sca}^{\lambda_l} R_{\lambda_l}(N) + \varepsilon f N \tag{5.16}$$

with $\forall\, 1 \leq l \leq G$

$$W_{\lambda_l}(N) \approx \sum_{i=0}^{S} w_i \left(\sum_{j=0}^{K} (2j+1) \left(d^-_{\lambda,j}(x_i, N)\, l^-_{\lambda,j}(x_i, N) + d^+_{\lambda,j}(x_i, N)\, l^-_{\lambda,j}(x_i, N) \right) \right),$$

$$R_{\lambda_l}(N) \approx \sum_{i=0}^{S} w_i \left(\sum_{j=0}^{K} (2j+1) \left(d^-_{\lambda_l,j}(x_i, N)\, B_{\lambda,j}(x_i, N) + d^+_{\lambda,j}(x_i, N)\, C_{\lambda,j}(x_i, N) \right) \right),$$

where ω_i is the weights, and $\forall\, 0 \leq i \leq S$, $\forall\, 0 \leq j \leq K$

$$B_{\lambda,j}(x_i, N) \approx \sum_{n=0}^{K} (2n+1)(\tilde{\Gamma}^{\beta,\beta}_{\lambda,j,n}\, l^-_{\lambda,j}(x_i, N) + \tilde{\Gamma}^{\alpha,\beta}_{\lambda,j,n}\, l^+_{\lambda,j}(x_i, N)),$$

$$C_{\lambda,j}(x_i, N) \approx \sum_{n=0}^{K} (2n+1)(\tilde{\Gamma}^{\alpha,\beta}_{j,n}\, l^-_{\lambda,j}(x_i, N) + \tilde{\Gamma}^{\alpha,\alpha}_{\lambda,j,n}\, l^+_{\lambda,j}(x_i, N)),$$

where $l^+_{\lambda,j}$, $l^-_{\lambda,j}$ are defined in (5.12), and $\tilde{\Gamma}^{u,v}_{\lambda,j,n}$ are defined by:

$$\forall j \geq 0, \forall n \geq 0, \tilde{\Gamma}^{u,v}_{\lambda,j,n} \equiv \tilde{\Gamma}^{u,v}_{\lambda,j,n}(r) = \sum_{k=0}^{K} \tilde{A}_{\lambda,k}(r)\, u_{k,j}\, v_{k,n},$$

with $\tilde{A}_{\lambda,k}$ is defined in (5.4), and u, v are defined in (5.13).

5.4. Iterative minimization algorithm

The purpose of this part is to present and analyze a numerical algorithm to approximate the solution of the previously studied minimization problem (4.4)-(4.5). We consider the Barzilai-Borwein minimization algorithm [9]:

$$\begin{cases} N_0, N_1 \quad \text{given}, N_0 \neq N_1, \\ g_0 = \nabla J_\varepsilon(N_0) \quad \text{and} \quad g_1 = \nabla J_\varepsilon(N_1), \end{cases}$$

and for all $n \geq 1$

$$\begin{cases} \Delta N_{n-1} = N_n - N_{n-1} \quad ; \quad \Delta g_{n-1} = g_n - g_{n-1}, \\ N_{n+1} = N_n - \dfrac{(\Delta N_{n-1}, \Delta g_{n-1})_{\mathcal{H}(\mathbb{R}^+)}}{(\Delta g_{n-1}, \Delta g_{n-1})_{\mathcal{H}(\mathbb{R}^+)}}\, g_n, \\ g_{n+1} = \nabla J_\varepsilon(N_{n+1}). \end{cases}$$

We also mention the conjugate gradient method [46], which is notably used by [51] in our context.

6. Numerical study of the stationary radiative transfer equation discretization

In this section, we study the numerical approximations presented in Section 5 with an analysis of their convergence on the explicit cases given in Section 3.2. We start by a nondimensionalization step in order to reduce the number of parameters.

6.1. Nondimensionalization of the radiative transfer equation

The first step is to normalize in (3.4) the spatial domain $[0, D]$ by $[0, 1]$ thanks to the change of variable $\tilde{x} = x/D$. Introducing the new functions:

$$\tilde{L}(x,\mu) = L(\tilde{x},\mu),\ \ \tilde{q}_\lambda(x,\mu) = q_\lambda(\tilde{x},\mu),\ \ \tilde{\sigma}^\lambda_{sca} = D\sigma^\lambda_{sca},\ \ \tilde{\sigma}^\lambda_{abs} = D\sigma^\lambda_{abs},\ \ \tilde{\sigma}^\lambda_{ext} = D\sigma^\lambda_{ext}, \tag{6.1}$$

then $\tilde{L}$ is the solution to:

$$\begin{cases} \mu\dfrac{\partial \tilde{L}_\lambda}{\partial x}(x,\mu,N) + \tilde{\sigma}^\lambda_{ext}(N)\tilde{L}_\lambda(x,\mu,N) = \tilde{\mathcal{K}}\tilde{L}_\lambda(x,\mu,N) + \tilde{q}_\lambda(x,\mu),\ (x,\mu)\in X \\ \tilde{L}_\lambda(0,\mu,N) = L^+_\lambda(\mu) \quad \text{for} \quad \mu>0 \quad \text{and} \quad \tilde{L}_\lambda(1,\mu,N) = L^-_\lambda(\mu) \quad \text{for} \quad \mu<0, \end{cases} \tag{6.2}$$

where $X = [0,1]\times([-1,0)\cup(0,1])$ and:

$$\tilde{\mathcal{K}}\tilde{L}_\lambda(x,\mu,N) = \frac{\tilde{\sigma}^\lambda_{sca}(N)}{2}\int_{-1}^{1}\Phi_\lambda(\mu,\mu',N)\,\tilde{L}_\lambda(x,\mu',N)\,d\mu'. \tag{6.3}$$

As mentioned in Section 1, we will focus our numerical experiments on a Lambertian source, leading to put, without loss of generality:

$$\forall\,\mu>0,\ L^+_\lambda(\mu) = 1. \tag{6.4}$$

Moreover, choosing D large enough, we will use the following boundary condition in all the sequel:

$$\forall\,\mu<0,\ L^-_\lambda(\mu) = 0. \tag{6.5}$$

In order to lighten the notations, all tildes will be omitted and $D = 1$.

6.2. Convergence error w.r.t. spatial discretization and Legendre series truncation

The case of the Beer-Lambert solution (Section 3.2.1) is investigated here in order to analyze the convergence of our numerical procedure of Section 5. Considering the problem (6.2) with $\tilde{\mathcal{K}} = 0$, $\tilde{q}_\lambda = 0$ and with boundary conditions (6.4)- (6.5), the solution is then given by (3.7):

$$L(x,\mu) = \begin{cases} \exp(-\sigma_{ext}x/\mu) & \text{if } \mu>0 \\ 0 & \text{if } \mu\le 0, \end{cases} \tag{6.6}$$

For a stepsize Δx defining a partition $0 = x_0 < x_1 < \cdots < x_N = 1$ and a number K of keeped terms in the Legendre series truncation, we denote by $L^K_{\Delta x}$ the approximate radiance of L obtained by the numerical method of Section 5. The cost function defined in (4.6) requiring the calculation of $\int_a^b L(x,\mu)dx$, we consider the following numerical error:

$$E(\sigma_{ext},K,\Delta x) = \sup_{0\le i\le N}\frac{\left|\int_a^b\left(L(x_i,\mu)d\mu - L^K_{\Delta x}(x_i,\mu)\right)d\mu\right|}{\int_a^b L(x_i,\mu)d\mu}. \tag{6.7}$$

For the numerical simulations, we will use, as in Section 7:

$$a = \cos\left(\frac{\pi}{360}\right), \quad b = 1 \text{ (forescattering measurement with } 1^{\text{o}} \text{ aperture angle)}. \tag{6.8}$$

We plot in Figure 6 the relative error (6.7) for the following values:

$$\sigma_{ext} \in \{6.25 \times 10^{-2}, 1.0, 4.0, 16.0\},\ K \in \{10, 30, 50, 70, 90\},\ \Delta x \in \{2^{-i},\ 5 \leq i \leq 18\}. \tag{6.9}$$

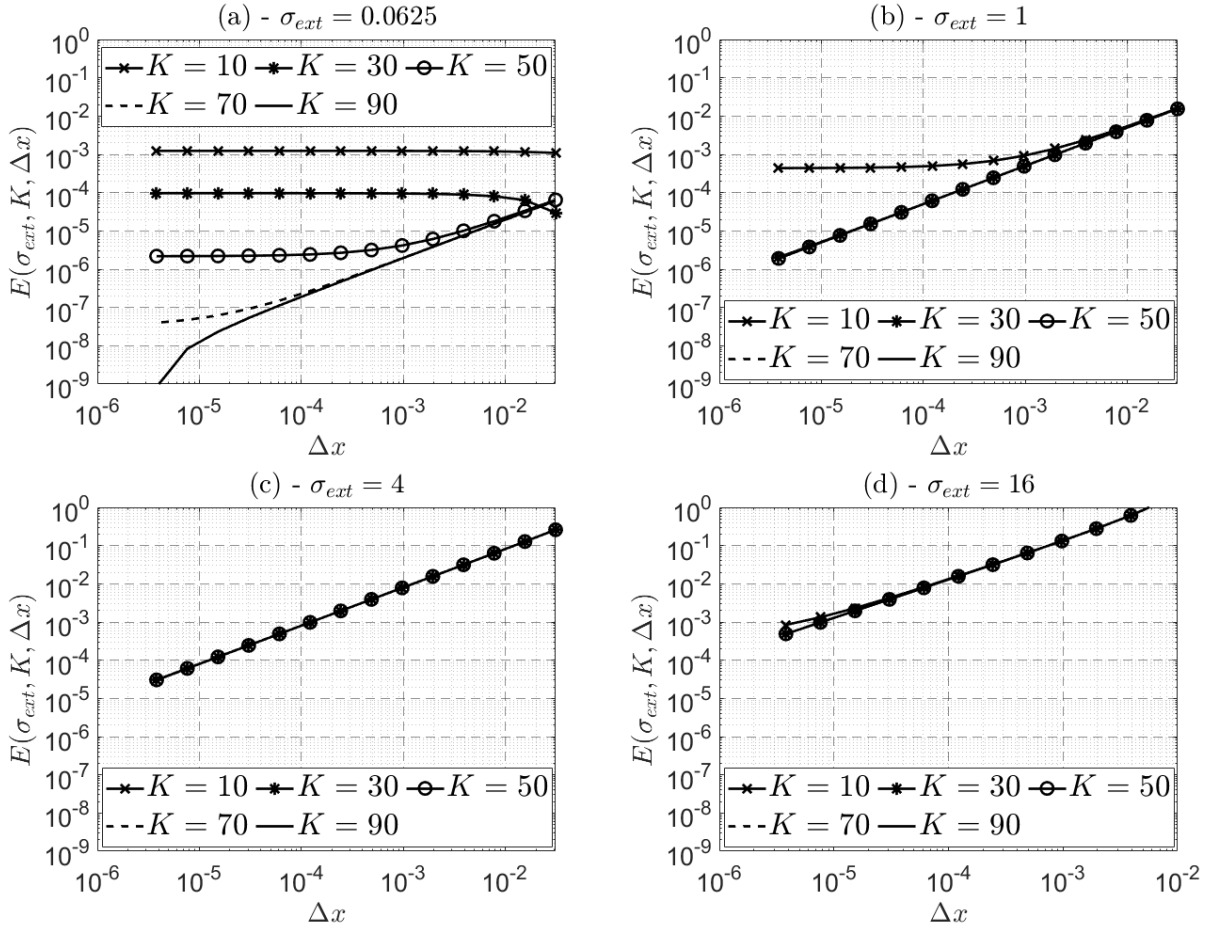

Figure 6: Error (6.7) in the Beer-Lambert case with σ_{ext} equal to $6.25\times\ 10^{-2}$ (a) , 1.0 (b), 4.0 (c) and 16.0 (d).

We can observe in Figure 6 that the error decreases as the step Δx decreases and as the truncation threshold K increases. The sensitivity to K is nevertheless very low for high extinction coefficients.

For the general case ($\mathcal{K} \neq 0$), we plot in Figure 7 the relative error (6.7). The calculations are done with one of the DSD of Figure 5(a). The "exact" solution, which is unknown, is assumed to be given by $L^K_{\Delta x}$ with $K = 100$ and $\Delta x = 2^{-18} \simeq 3.8 \times 10^{-6}$.

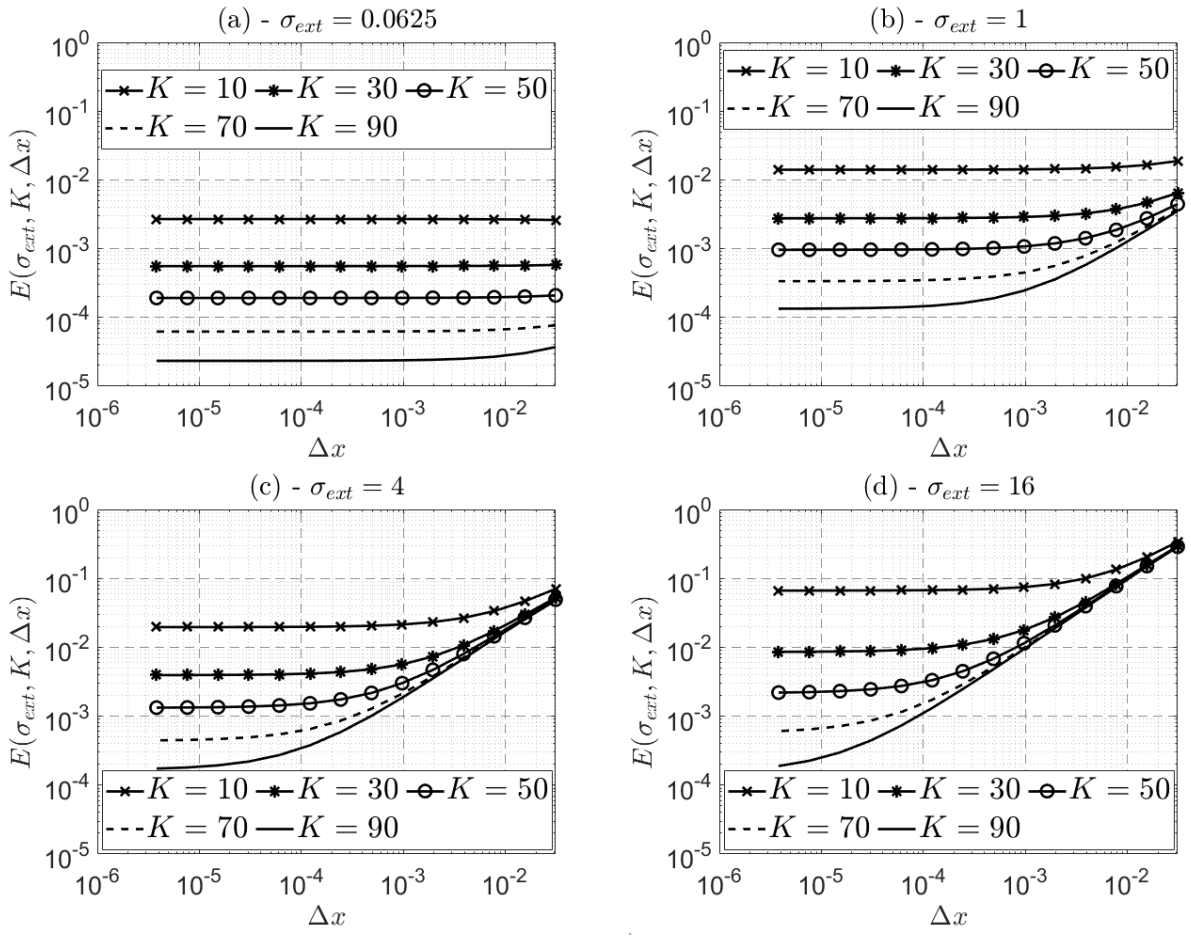

Figure 7: Error (6.7) in the general case with σ_{ext} equal to $6.25\times\ 10^{-2}$ (a) , 1.0 (b), 4.0 (c) and 16.0 (d).

We can observe in Figure 7 a higher sensitivity to K, especially if the stepsize Δx is small. We will keep in the sequel:

$$K = 50 \text{ and } \Delta x = 10^{-3} \Longrightarrow E(\sigma_{ext}, k, \Delta x) \leq 10^{-2}. \tag{6.10}$$

We end this study by plotting in Figure 8 the numerical and explicit radiance with respect to x and μ with $\Delta x = 10^{-3}$, and 50 Legendre polynomials, for the Beer-Lambert case and the collision case (in this latter, the explicit solution is given by $L^K_{\Delta x}$ with $K = 100$ and $\Delta x = 2^{-18} \simeq 3.8 \times 10^{-6}$).

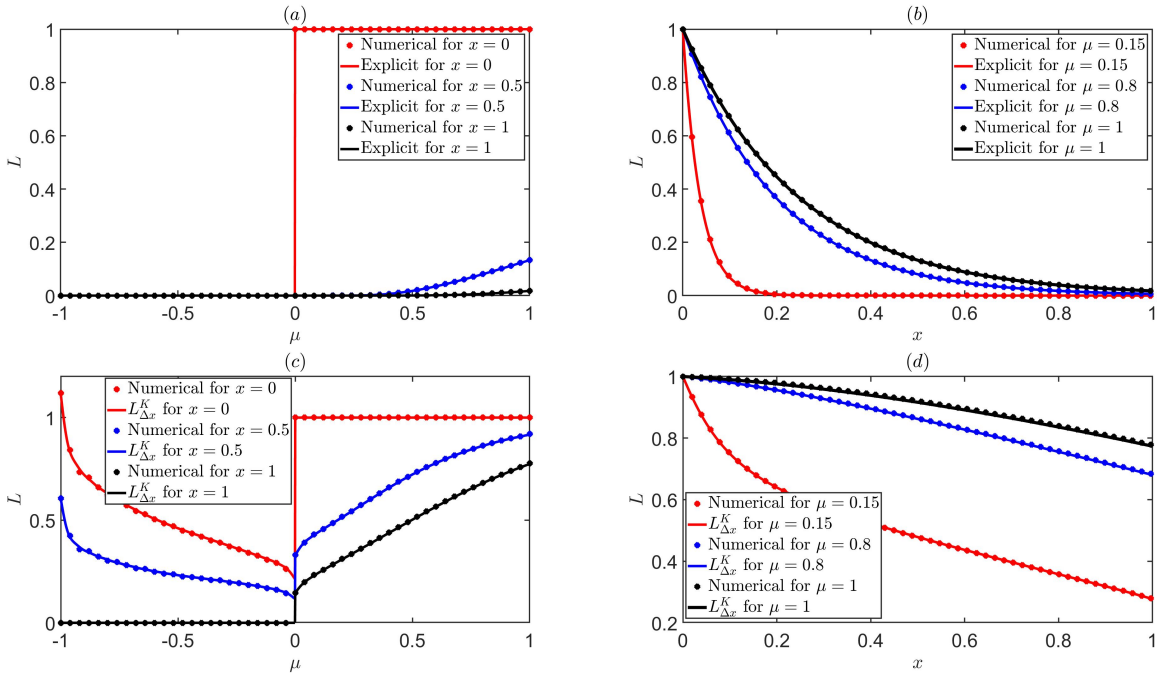

Figure 8: Numerical and explicit radiances with respect to x and μ with $\Delta x = 10^{-3}$, and 50 Legendre polynomials, for the Beer-Lambert case ((a) and (b)) and the collision case ((c) and (d)).

6.3. Study for the adjoint problem of the RTE

The adjoint problem (4.9) involves Dirac sources. We apply our numerical scheme on the simple model (3.8) whose solution is given by (3.9). We then consider the following problem:

$$\begin{cases} \mu \dfrac{\partial L}{\partial x}(x,\mu) + \sigma L(x,\mu) = \delta_{1/2}(x),\ 0 < x < 1,\ -1 < \mu < 1 \\ L(0,\mu) = L(1,-\mu) = 0,\ \mu > 0, \end{cases} \tag{6.11}$$

whose solution is given by:

$$L(x,\mu) = \frac{1}{|\mu|} e^{\sigma(x-1/2)/\mu}\, \mathbb{1}_{(x-1/2)\mu>0}(\mu). \tag{6.12}$$

We plot in Figure 9(a) the numerical and explicit radiances with respect to x and μ with $\Delta x = 10^{-3}$, and 50 Legendre polynomials for the problem (6.11) with $\sigma = 4.0$. We can observe a very good agreement between numerical and explicit solutions. In order to take into account a collision operator which appears in the adjoint problem, we consider the Dautray-Lions solution (3.11) of problem (3.10). Since the Dautray-Lions solution (3.11) does not give the radiance but its integral over μ, we consider the following numerical error associated to the discretization of (3.10):

$$E(\Delta x, K, c) = \frac{\left| \int_{\mathbb{R}} \int_{-1}^{1} \left(L(x,\mu) - L^K_{\Delta x}(x,\mu) \right) d\mu dx \right|}{\int_{\mathbb{R}} \int_{-1}^{1} L(x,\mu) d\mu}, \tag{6.13}$$

where c is the parameter of the Dautray-Lions problem. We plot in Figure 9(b) the numerical and explicit function T (see 3.11) with respect to x with $\Delta x = 10^{-3}$, and 50 Legendre

polynomials for the problem (3.10) with $c = 0.5$. In this case, we then find $E(2^{-16}, 100, 0.5) = 3.53 \times 10^{-2}$.

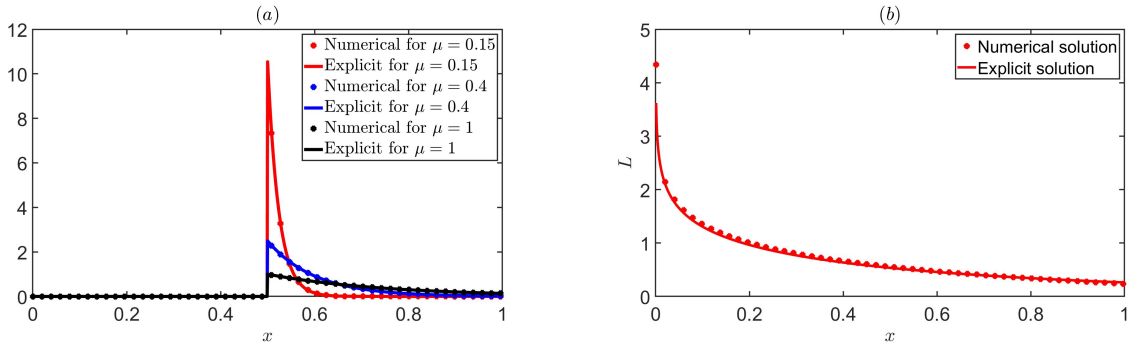

Figure 9: Numerical and explicit radiances with respect to x and μ with $\Delta x = 10^{-3}$, and 50 Legendre polynomials for the problem (6.11) with $\sigma = 4.0$ (a). Numerical and explicit function T (see 3.11) w.r.t. x with $\Delta x = 10^{-3}$ and 50 Legendre polynomials for the problem (3.10) with $c = 0.5$.

7. Droplet size distribution identification results

In this part, we present some numerical identification of the distribution N by using synthetic measurements. We investigate the reconstruction method for different radiative transfer modellings and for the 3 types of DSD presented in Figure 5. The identification is done in the following four cases:

1. Beer-Lambert case with forescattering measurements ($\theta' = 0°$ and $\alpha = 1°$);
2. Isotropic collision operator case with forescattering measurements ($\theta' = 0°$ and $\alpha = 1°$);
3. Isotropic collision operator case with backscattering measurements ($\theta' = 180°$ and $\alpha = 1°$);
4. Anisotropic collision operator case with backscattering measurements ($\theta' = 180°$ and $\alpha = 1°$).

From a target distribution function, noted $N^\star$, the measurements are reconstructed as follows:

$$\forall\, 1 \leq i \leq I,\ 1 \leq l \leq G, \quad M_{\lambda_l}(x_i) = \int_a^b L^\star_{\lambda_l}(x_i, \mu, N^\star)\, d\mu \tag{7.1}$$

for $I = 1$, $x_1 = 0.5$ (forescattering), $x_1 = 0$ (backscattering) and for $G = 50$ wavelengths equally distributed between $300\, nm$ and $2500\, nm$:

$$\forall\, 1 \leq l \leq 50,\ \lambda_l = 300 + 44 * (l - 1)\ \text{nm}. \tag{7.2}$$

In order to study the convergence of the minimization algorithm, we calculate at each iteration k the relative error RE of the minimizer and the relative cost RC

$$\begin{cases} RE(k) = \sqrt{\dfrac{(N_k - N^\star, N_k - N^\star)_{\mathcal{H}(\mathbb{R}^+)}}{(N^\star, N^\star)_{\mathcal{H}(\mathbb{R}^+)}}} = \dfrac{\left(\displaystyle\sum_{i=1}^{R} [r_i(N_k(r_i) - N^\star(r_i))]^2\right)^{1/2}}{\left(\displaystyle\sum_{i=1}^{R} (r_i N^\star(r_i))^2\right)^{1/2}} \\ RC(k) = \dfrac{J_1(N_k)}{J_1(N_0)} \end{cases}$$

where R denotes the number of sub-intervals which the particle size range $[r_{min}, r_{max}]$ is divided into; J_1 is defined in (4.6), $N^\star$ is the target DSD and N_0 is the initial DSD for the minimization algorithm. This algorithm is initialized by the two vectors $N_0 = (1, \cdots, 1)$ and $N_1 = N_0 - 0.1\,\nabla J_\varepsilon(N_0)$ in all the numerical results shown in this section. The actual measurements have a noise level η, such as:

$$\forall\, \lambda \in [300\, nm, 2500\ nm],\ \|M_\lambda^\eta - M_\lambda\|_{L^\infty([0,D])} \leq \eta$$

where

$$M_\lambda^\eta = (1 + \eta\, U) M_\lambda$$

represents the measurements (with a relative noise level $\eta \geq 0$ and U a random variable with uniform law on $(0, 1)$) and M_λ represents the true measurements corresponding to the target distribution $N^\star$.
We perform our simulations with a Lambertian source, where the radiance at $x = 0$ is constant and is independent of μ (i.e we take $L(0, \mu) = L^+(\mu) = 1$ and $L(D, \mu) = L^-(\mu) = 0$). We fix two choices for the couple $(\varepsilon, f(r))$ depending on the locations of the DSD's peak. We refer to Table 3 for the $(\varepsilon, f(r))$ choices after some preliminar experiments.

Conditions	ε	$f(r)$
DSD with a peak location $r_m < 1\,\mu$m	10^{-14}	$1/r^9$
DSD with a peak location $r_m > 1\,\mu$m	10^{-6}	$1/r^4$

Table 3: Choices of the (ε, f) parameters of the cost function.

7.1. Determination of the best descent algorithm

We determine the descent algorithm having the best performances by a comparison on the Beer-Lambert modelling case (see Section 3.2.1). Forescattering measurements are carried out ($\theta' = 0°, \alpha = 1°$). We recall, for all $\varepsilon \geq 0$, the cost function:

$$J_\varepsilon(N) = \frac{1}{2} \sum_{i=1}^{I} \sum_{l=1}^{G} \left(\frac{\displaystyle\int_a^b e^{-\sigma_{ext}^{\lambda_l}(N)\,\frac{x_i}{\mu}}\, d\mu - M_{\lambda_l}(x_i)}{M_{\lambda_l}(x_i)} \right)^2 + \frac{\varepsilon}{2} \|\sqrt{f} N\|^2_{\mathcal{H}(\mathbb{R}^+)}. \tag{7.3}$$

In this case (Beer-Lambert explicit solution to the RTE), we can simply compute the gradient of J_ε:

$$DJ_\varepsilon(N)\cdot\overline{N} = -\sum_{l=1}^{G}\sigma_{ext}^{\lambda_l}(\overline{N})\left(\sum_{i=1}^{I} x_i\, B^{\lambda_l}(x_i)\int_a^b \frac{1}{\mu}e^{-\sigma_{ext}^{\lambda_l}(N)\frac{x_i}{\mu}}\,d\mu\right) + \varepsilon\int_0^{+\infty} r^2 f(r)N(r)\overline{N}(r)\,dr \quad (7.4)$$

with

$$B^{\lambda_l}(x_i) = \left(\frac{\displaystyle\int_a^b e^{-\sigma_{ext}^{\lambda_l}(N)\frac{x_i}{\mu}}\,d\mu - M_{\lambda_l}(x_i)}{(M_{\lambda_l}(x_i))^2}\right),\ 1\le i\le I\,;\ 1\le l\le G.$$

We then obtain:

$$\nabla J_\varepsilon(N) = -\pi\sum_{l=1}^{G} Q_{ext}^{\lambda_l}\left(\sum_{i=1}^{I} x_i\, B^{\lambda_l}(x_i)\int_a^b \frac{1}{\mu}\,e^{-\sigma_{ext}^{\lambda_l}(N)\frac{x_i}{\mu}}\,d\mu\right) + \varepsilon\, f\, N. \quad (7.5)$$

A Gauss's integration formula is used to compute the integral in (7.5).

A comparison between the Barzilai-Borwein minimization algorithm and the two conjugate gradient algorithms CG-Polak Ribiere and CG-Daniel [46] is shown in Figure 10 for one of the DSD of Figure 5(a).

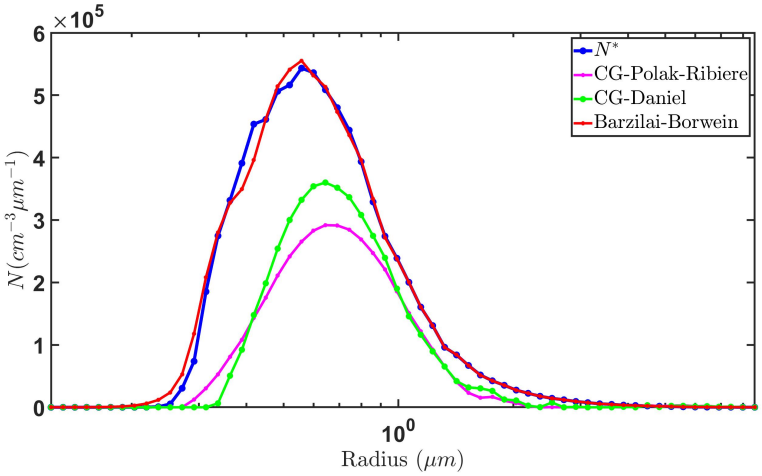

Figure 10: Reconstructed DSDs obtained by Barzilai-Borwein, CG-Polak Ribiere and CG-Daniel minimization algorithms after 30 000 iterations, and PAVIN platform target DSD with $\theta' = 0°$, $\alpha = 1°$, $x = 0.5$ and $\eta = 0\%$.

Methods	$J_1(N)$	relative cost	relative error
Barzilai-Borwein	8.478×10^{-10}	7.263×10^{-13}	2.555×10^{-2}
CG-Polak Ribiere	3.816×10^{-6}	1.228×10^{-4}	4.052×10^{-1}
CG-Daniel	1.253×10^{-6}	4.035×10^{-5}	3.217×10^{-1}

Table 4: The cost J_1, the relative cost RC, and the relative error RE, after 30 000 iterations for various minimization algorithms with $\varepsilon = 10^{-14}$ and $f(r) = \frac{1}{r^9}$.

After 30 000 iterations, from Table 4 and in comparison to $N^\star$, our approximated N by the Barzilai-Borwein algorithm has an error of 2.5%, is less than the error obtained by CG-Polak Ribiere algorithm 40% and CG-Daniel algorithm 32%. Figure 10 confirms that the identification of the distribution N by the Barzilai-Borwein algorithm is the best among the three algorithms used. We give in Table 5 the relative error:

$$E_\lambda^2 = \frac{\|L_\lambda^\star - L_\lambda^a\|_{L^\infty(X)}}{\|L_\lambda^\star\|_{L^\infty(X)}}$$

between the radiance $L_\lambda^\star$ calculated from $N^\star$, and the radiance L_λ^a calculated from the approximated N by the Barzilai-Borwein algorithm.

$\lambda\,(nm)$	300	500	1000	1500	2000	2500
E_λ^2	2.284×10^{-5}	1.174×10^{-4}	5.496×10^{-5}	3.735×10^{-5}	2.250×10^{-5}	9.236×10^{-6}

Table 5: Relative error E_λ^2 between the radiance calculated by $N^\star$ and by the approximated N (obtained by BB algorithm) w.r.t. wavelength λ.

We observe a very small difference between the spectral radiance calculated from target $N^\star$ and the approximated N. In the sequel, we shall use the Barzilai-Borwein algorithm to identify the distribution N.

7.2. Beer-Lambert case

Figure 11 shows the identification results for various droplet size distributions measured at the Cerema PAVIN Platform. Table 6 presents the values of the relative cost and the relative error of these tests after 30 000 iterations, which suggest that the identification is satisfactory.

Tests	$J_1(N)$	relative cost	relative error
Test 1 (top left)	1.892×10^{-9}	8.597×10^{-12}	2.830×10^{-2}
Test 2 (top right)	1.312×10^{-10}	3.896×10^{-13}	1.492×10^{-2}
Test 3 (bottom left)	1.006×10^{-9}	1.627×10^{-12}	2.237×10^{-2}
Test 4 (bottom right)	2.965×10^{-10}	7.416×10^{-13}	2.105×10^{-2}

Table 6: The cost $J_1(N)$, the relative cost RC, and the relative error RE after 30 000 iterations with $\varepsilon = 10^{-14}$ and $f(r) = \frac{1}{r^9}$ corresponding to Figure 11.

Figure 12 shows the identification results for various droplet size distributions measured on Paris-Fog campaign [11] (see Figure 5(b)). Table 7 presents the values of the relative cost

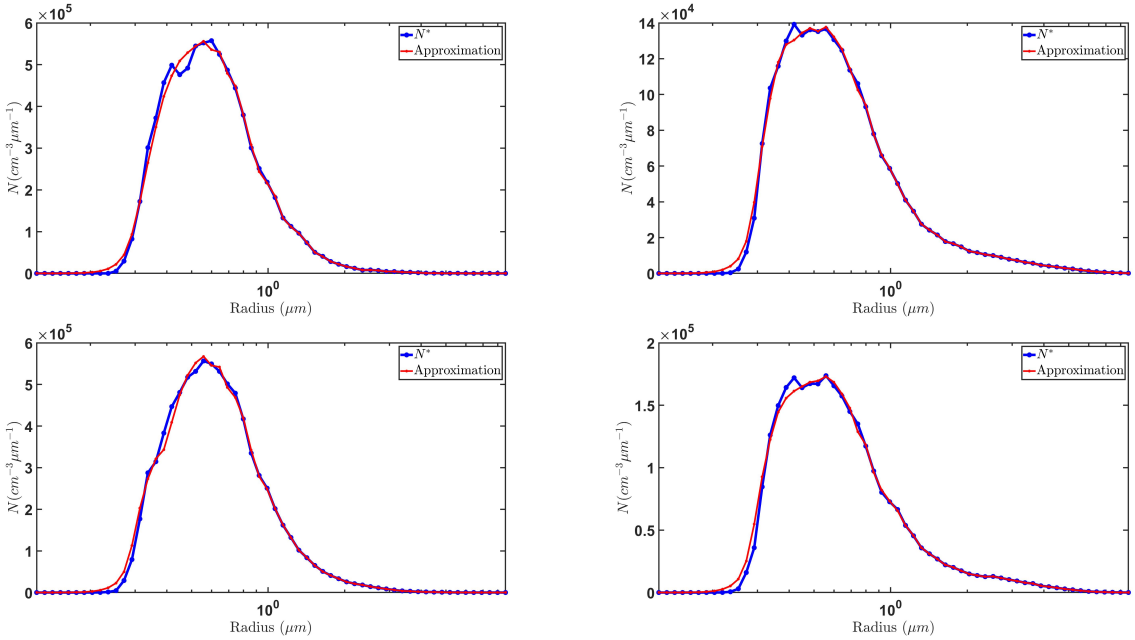

Figure 11: Identification results obtained after 30 000 iterations with $\theta' = 0°$, $\alpha = 1°$, $x = 0.5$ and the noise $\eta = 0\%$ for 4 PAVIN platform DSDs.

and the relative error of these tests after 100 000 iterations. These figures and this table suggest that the identification is satisfactory with an error ranging between 4,7% or 8%.

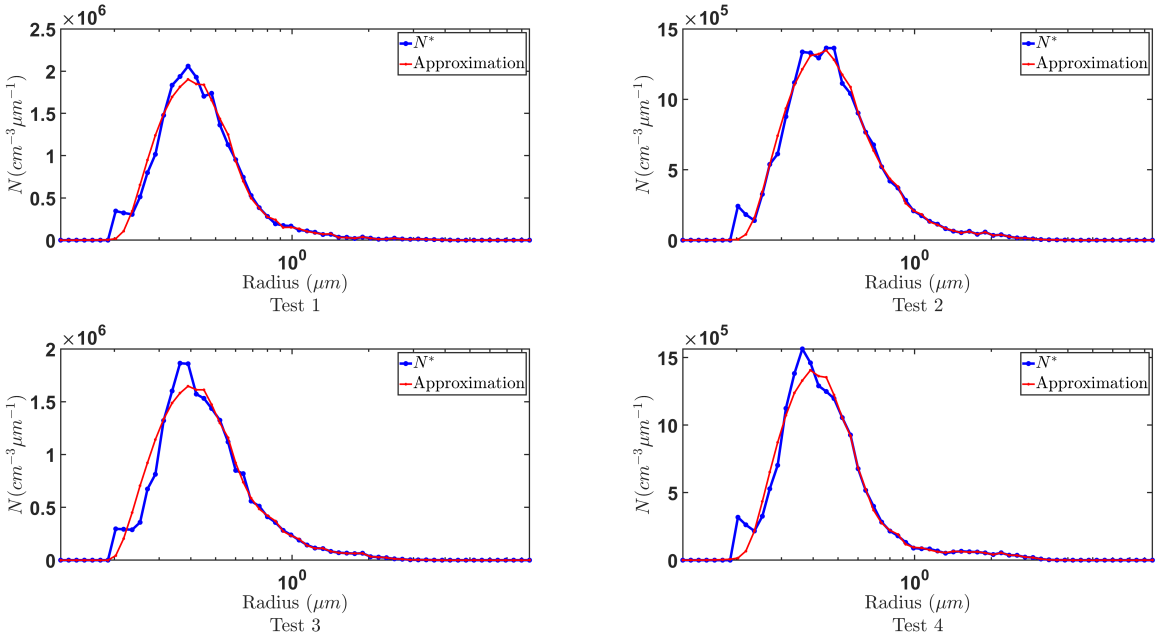

Figure 12: Identification results obtained after 100 000 iterations with $\theta' = 0°$, $\alpha = 1°$, $x = 0.5$ and the noise $\eta = 0\%$ for 4 Paris-Fog DSDs.

Tests	$J_1(N)$	relative cost	relative error
Test 1 (top left)	2.0137×10^{-7}	3.325×10^{-10}	7.614×10^{-2}
Test 2 (top right)	4.924×10^{-8}	6.379×10^{-11}	4.743×10^{-2}
Test 3 (bottom left)	3.917×10^{-7}	5.377×10^{-10}	8.190×10^{-2}
Test 4 (bottom right)	1.410×10^{-7}	1.523×10^{-10}	7.048×10^{-2}

Table 7: The cost $J_1(N)$, the relative cost RC, and the relative error RE after 100 000 iterations with $\varepsilon = 10^{-14}$ and $f(r) = \frac{1}{r^9}$ corresponding to Figure 12.

We now test the method on the Shettle and Fenn models of Table 1. The identification results are presented in Figure 13. Table 8 shows the relative cost and the relative error of the identifications presented in Figure 13.

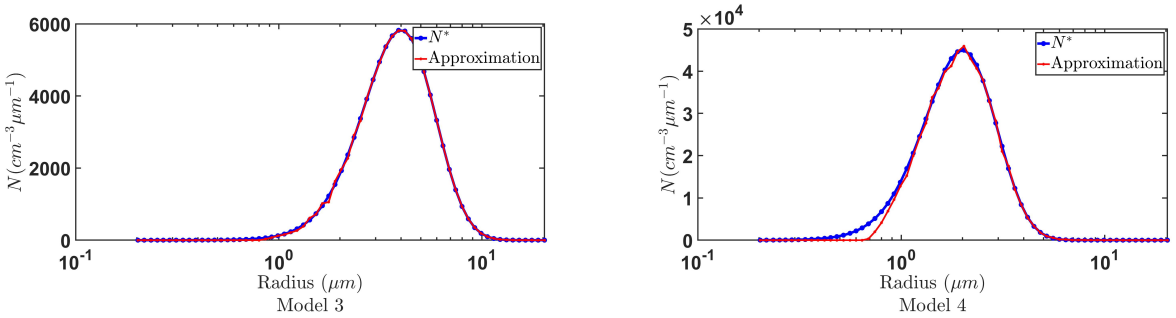

Figure 13: Identification results obtained after 10 000 iterations with $\theta' = 0°$, $\alpha = 1°$, $x = 0.5$ and the noise $\eta = 0\%$ for Shettle and Fenn DSD models.

Tests	$J_1(N)$	relative cost	relative error
Model 3 (left)	4.723×10^{-9}	4.680×10^{-8}	4.333×10^{-3}
Model 4 (right)	6.828×10^{-6}	1.099×10^{-6}	2.690×10^{-2}

Table 8: The cost $J_1(N)$, the relative cost RC, and the relative error RE after 10 000 iterations with $\varepsilon = 10^{-6}$ and $f(r) = \frac{1}{r^4}$.

7.3. Isotropic collision operator case

We introduce here a collision operator in the radiative transfer modelling thanks to the isotropic phase function $\Phi_\lambda \equiv 1$ and we then apply the DSD reconstruction method. Note that this case does not have a very physical meaning since we prescribe a given phase function when it should depend on the DSD. Nevertheless, it has the merit of testing our method in a more complex case than the Beer-Lambert case allowing to consider backscattering measurements. According to Figure 14, we observe a good approximation of $N^\star$ with either forescattering or backscattering measurements with a relative cost less than 10^{-7} and a relative error less than 5 %.

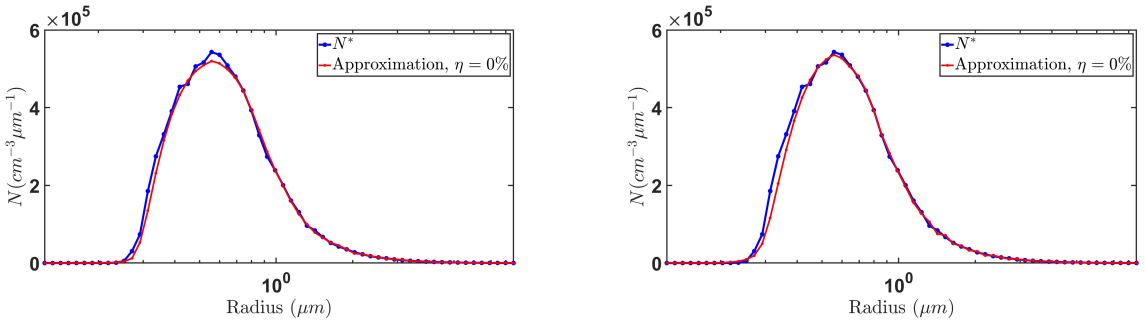

Figure 14: Identification results obtained after 2 000 iterations with forescattering measurements (left) and backscattering measurements (right) for a PAVIN platform DSD.

Measurement type	$J_\varepsilon(N)$	relative cost	relative error
Forescattering	4.980×10^{-7}	7.514×10^{-8}	$3.432\times\ 10^{-2}$
Backscattering	7.444×10^{-7}	2.985×10^{-8}	$4.164\times\ 10^{-2}$

Table 9: The cost $J_\varepsilon(N)$, the relative cost RC, and the relative error RE after 2000 iterations for forescattering and backscattering measurements in the isotropic case.

7.4. Anisotropic collision operator case

In this part, we identify the distribution N in the anisotropic case when the phase function in the collision operator is calculated from the distribution N. From aour numerical testing, the forescattering measurements do not properly identify the droplet size distribution. However, backscattering measurements allow to well reconstruct the DSD. Figure 15 shows the identification of DSD in backscattering measurements after 5000 iterations. The peak of 0.5 μm is reached. Table 10 shows a relative cost less than 10^{-7} and a relative error around than 7 % (slightly larger than in the isotropic case).

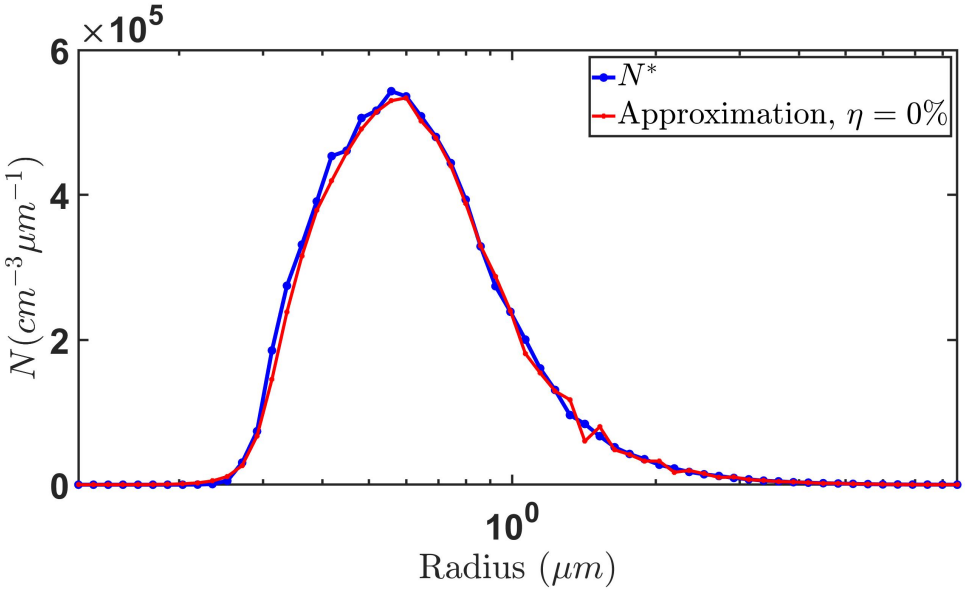

Figure 15: Identification results obtained after 5 000 iterations with backscattering measurements (right) for a PAVIN platform DSD in the anisotropic case.

Measurement type	$J_\varepsilon(N)$	relative cost	relative error
Backscattering	1.212×10^{-6}	5.143×10^{-8}	$7.244\times\ 10^{-2}$

Table 10: The cost $J_\varepsilon(N)$, the relative cost RC, and the relative error RE after 5000 iterations backscattering measurements in the anisotropic case.

7.5. Noise adding on the measurements

To study the robustness of the DSD identification method, we add to the measurements a noise level of 1% and 3%. We gather in Figure 16 the reconstructed DSD with different noises for the following cases: forescattering and backscattering measurements in isotropic conditions and backscattering measurements in anisotropic conditions. Table 11 details values of the cost $J_\varepsilon(N)$, the relative cost RC and the relative error RE for different modellings, measurement types and noise levels on the measurements. According to Figure 16, the identification results are correct for 1% noise level: in particular, the peak at 0.5 μm is reached. For a 3% noise level, the reconstruction begins to change.

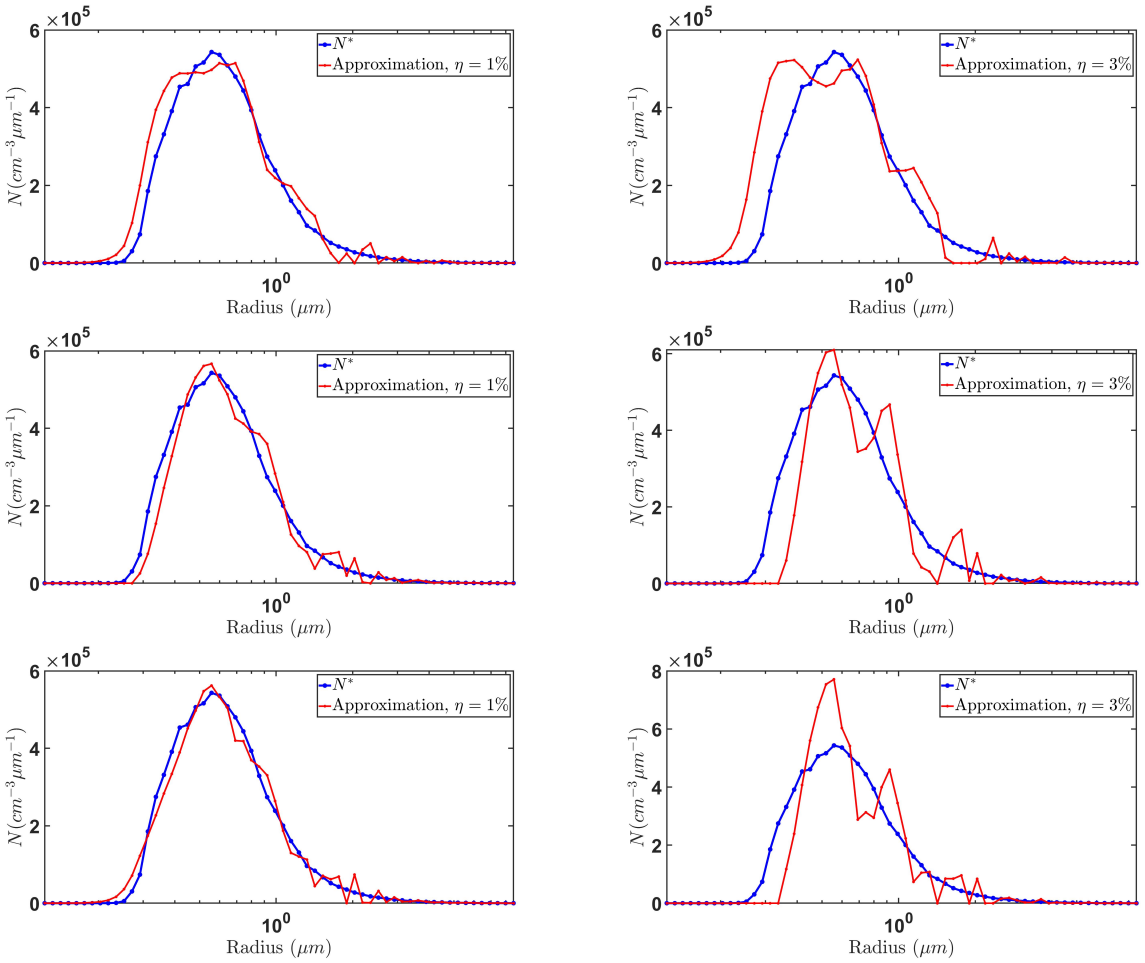

Figure 16: Identification results with noise adding (1% on the left, 3% on the right) in forescattering and isotropic case (first line), backscattering and isotropic case (second line) and backscattering and anisotropic case (third line).

Modelling	Measurement type	Noise η	$J_\varepsilon(N)$	relative cost	relative error
Isotropic	Forescattering	0 %	4.980×10^{-7}	7.514×10^{-8}	$3.432\times\ 10^{-2}$
Isotropic	Forescattering	1 %	6.020×10^{-4}	9.089×10^{-5}	2.580×10^{-1}
Isotropic	Forescattering	3 %	6.166×10^{-3}	9.297×10^{-4}	4.100×10^{-1}
Isotropic	Backscattering	0 %	7.444×10^{-7}	2.985×10^{-8}	$4.164\times\ 10^{-2}$
Isotropic	Backscattering	1 %	5.251×10^{-4}	2.106×10^{-5}	$2.550\times\ 10^{-1}$
Isotropic	Backscattering	3 %	5.394×10^{-3}	2.163×10^{-4}	$5.087\times\ 10^{-1}$
Anisotropic	Backscattering	0 %	1.212×10^{-6}	5.143×10^{-8}	$7.244\times\ 10^{-2}$
Anisotropic	Backscattering	1 %	5.118×10^{-4}	2.171×10^{-5}	$2.511\times\ 10^{-1}$
Anisotropic	Backscattering	3 %	5.217×10^{-3}	2.212×10^{-4}	$4.608\times\ 10^{-1}$

Table 11: The cost $J_\varepsilon(N)$, the relative cost RC and the relative error RE for different modellings, measurement types and noise levels on the measurements.

For 1% and 3% noise levels on the measurements, the reconstructed N has respectively about 25% error and 50% with the target DSD $N^\star$. We can observe the same behavior for

the gap between the approximation N_{app}^{η} obtained with a noise η and the approximation N_{app}^{0} with $\eta = 0$:

$$\text{Gap} = \frac{\|N_{app}^{\eta} - N_{app}^{0}\|_{\mathcal{H}(\mathbb{R}^+)}}{\|N_{app}^{0}\|_{\mathcal{H}(\mathbb{R}^+)}} \tag{7.6}$$

Table 12 shows the gap (7.6) obtained on the approximated N with respect to the noise level applied on the measurements.

Modelling	Measurement type	Noise η on M_λ	Gap on N
Isotropic	Backscattering	1%	24.08 %
Isotropic	Backscattering	3%	44.17 %
Anisotropic	Backscattering	1%	21.77 %
Anisotropic	Backscattering	3%	38.44 %

Table 12: The gap obtained on N in function of the noise applied on M_λ.

8. Conclusion

The droplet size distribution (DSD) in a fog or cloud has an impact on the optical properties of the medium and its knowledge is therefore necessary to take into account clouds or fogs in meteorological models for example. We developped this work of identifying DSDs for another application than meteorology, namely the evaluation of optical sensors such as cameras, radars or lidars in adverse weather conditions for applications to intelligent transport systems. We proposed an identification method based on radiation measurements at different wavelengths in the 0 nm -2500 nm spectral band and the inversion of radiative transfer models. We assumed that the medium in which the measurements were made could be considered as optically homogeneous and that the radiative transfer within it could be modelled by a one-dimensional space equation. We then considered a complete modelling of the radiative transfer equation by taking into account a collision operator provided by the DSD via the Mie theory.

A least-squares method combined with the Barzilai Borwein algorithm has been used to identify the droplet size distribution (DSD) from radiation measurements. The minimization of the cost function required to calculate its gradient with respect to the DSD, what was done thanks to the resolution of an adjoint problem to the radiative transfer equation. Inspired by Yvon's works, a decomposition method on the double Legendre basis has been used to approximate the stationary radiative transfer equation and its adjoint. The numerical method has been evaluated and validated on several explicit solutions of the stationary radiative transfer equation. In addition, an extensive numerical study was carried out to determine the convergence errors in the proposed numerical methods. A comparison between the Barzilai-Borwein algorithm and two algorithms based on the conjugate gradient was performed. It concluded that the Barzilai-Borwein method was more efficient than the other two and all numerical applications were performed with this algorithm. Various models describing fog DSDs (Shettel and Fenn) and real DSD measured in natural conditions (Paris Fog campaign) or in artificial conditions (Cerema PAVIN platform) are used to compute synthetic radiation measurements via Mie theory and the radiative transfer equation

under different assumptions (Beer-Lambert modelling, isotropic or anisotropic collision operator). Afterwards, the identification of the DSDs was carried out using these three radiative transfer modellings. In the Beer-Lambert case, the DSD reconstruction was successful by using forescattering measurements. In case of a modelling with an isotropic collision term, forescattering or backscattering measurements led to well reconstruct the DSD. From our numerical experiments, the identification method in the anisotropic case requires backscattering measurements. We explored in the last section the robustness of the method and constated that the DSD reconstruction is very sensitive with respect to the noise adding on measurements. For a 3% noise level, the identification is poorly approached.

Particle size distribution identifications are a wide area of research, and various issues remain unsolved that require additional investigation of light scattering theory and particle size distribution inversion approaches. Based on this present works, the inversion of fog particle size distributions using real measurements will be considered in further studies. We will also consider the case of 3D modelling which may be necessary to interpret the real measurements. Furthermore, it will be interesting to consider other types of sources such as collimated sources for example. Finally, other wavelengths such as thermal infrared could be considered to improve the method.

Acknowledgments

This work was supported by the International Research Center "Innovation Transportation and Production Systems" of the I-SITE CAP 20-25.

Appendix A. Gradient of the cost function

To compute the expression of the gradient of the cost function J_ε (4.5), we define the Lagrangian $\mathcal{L}$ as follows:

$$\begin{aligned}
\mathcal{L}(N,L,p) = \frac{1}{2}\sum_{i=1}^{I}\sum_{l=1}^{G}\left(\frac{\int_a^b L_{\lambda_l}(x,\mu,N)\,d\mu - M_{\lambda_l}(x_i)}{M_{\lambda_l}(x_i)}\right)^2 + \frac{\varepsilon}{2}\,\|\sqrt{f}N\|^2_{\mathcal{H}(\mathbb{R}^+)} \\
+\sum_{l=1}^{G}\left[\int_{-1}^{1}\int_0^H \mu\,\frac{\partial p}{\partial x}(x,\mu,N)L_{\lambda_l}(x,\mu,N)\;dx\,d\mu\right] \\
-\sum_{l=1}^{G}\left[\sigma_{ext}^{\lambda_l}(N)\int_{-1}^{1}\int_0^H p_{\lambda_l}(x,\mu,N)L_{\lambda_l}(x,\mu,N)\,dxd\mu\right] \\
+\sum_{l=1}^{G}\left[\int_{-1}^{1}\int_0^H p_{\lambda_l}(x,\mu,N)\int_{-1}^{1}L(x,\mu',N)f_\lambda(\mu,\mu',N)d\mu'dxd\mu\right] \\
-\sum_{l=1}^{G}\left[\int_0^1 \mu\,p_{\lambda_l}(D,\mu,N)\,L_{\lambda_l}(D,\mu,N)\,d\mu - \int_{-1}^{0}\mu\,p_{\lambda_l}(D,\mu,N)\,L^-_{\lambda_l}(\mu)\,d\mu\right] \\
+\sum_{l=1}^{G}\left[\int_{-1}^{0}\mu\,p_{\lambda_l}(0,\mu,N)\,L_{\lambda_l}(0,\mu,N)\,d\mu\right] \\
+\sum_{l=1}^{G}\left[\int_0^1 \mu\,p_{\lambda_l}(0,\mu,N)\,L^+_{\lambda_l}(\mu)\,d\mu\right]
\end{aligned} \tag{A.1}$$

where p_λ is the Lagrange multiplier that verifies (4.9) and

$$f_\lambda(\mu,\mu',N) = \frac{\sigma^\lambda_{sca}(N)}{2}\Phi_\lambda(\mu,\mu',N) = \frac{1}{4}\int_0^{2\pi}\int_0^{+\infty} Q^\lambda_{sca}(r)\psi_\lambda(r,\mu\mu'+\sqrt{1-\mu^2}\sqrt{1-\mu'^2}\cos(w))r^2N(r)drdw,$$

$$\sigma^{\lambda_l}_{ext}(N) = \pi\int_0^{+\infty} Q^\lambda_{ext}(r)\,r^2\,N(r)\,dr.$$

Let $N_\eta = N + \eta\overline{N}$ we have

$$L_\lambda(x,\mu,N_\eta) = L_\lambda(x,\mu,N) + \eta\overline{L}_\lambda(x,\mu,\overline{N}) + o(\eta^2).$$

By using (3.4) and

$$\mu\frac{\partial L_\lambda}{\partial x}(x,\mu,N_\eta) + \sigma^\lambda_{ext}(N_\eta)\,L_\lambda(x,\mu,N_\eta) = \int_{-1}^{1} L_\lambda(x,\mu',N_\eta)f(\mu,\mu',N_\eta)d\mu',$$

we obtain the following problem satisfied by $\overline{L}_\lambda$:

$$\begin{cases} \mu\dfrac{\partial \overline{L}_\lambda}{\partial x}(x,\mu,\overline{N}) + \sigma^\lambda_{ext}(\overline{N})\, L_\lambda(x,\mu,N) + \sigma^\lambda_{ext}(N)\, \overline{L}_\lambda(x,\mu,\overline{N}) = \displaystyle\int_{-1}^{1} L_\lambda(x,\mu',N) f_\lambda(\mu,\mu',\overline{N}) d\mu' \\ \qquad\qquad\qquad\qquad\qquad\qquad\qquad\qquad + \displaystyle\int_{-1}^{1} \overline{L}_\lambda(x,\mu',\overline{N}) f_\lambda(\mu,\mu',N) d\mu' \\ \overline{L}_\lambda(0,\mu,\overline{N}) = 0 \qquad if \quad \mu \in (0,1] \\ \overline{L}_\lambda(D,\mu,\overline{N}) = 0 \qquad if \quad \mu \in [-1,0). \end{cases} \tag{A.2}$$

But

$$DJ_\varepsilon(N)\cdot\overline{N} = \lim_{\eta\to 0}\frac{J_\varepsilon(N_\eta)-J_\varepsilon(N)}{\eta} = \varepsilon\int_{\mathbb{R}^+} r^2\, f(r)\, N(r)\, \overline{N}(r)\, dr + \sum_{i=1}^{I}\sum_{l=1}^{G} K(x_i,\lambda_l)\, \left(\int_a^b \overline{L}_{\lambda_l}(x_i,\mu,\overline{N}) d\mu\right) \tag{A.3}$$

where

$$K(x_i,\lambda_l) = \left(\frac{\displaystyle\int_a^b L_{\lambda_l}(x_i,\mu)\, d\mu - M_{\lambda_l}(x_i)}{(M_{\lambda_l}(x_i))^2}\right).$$

To simplify the gradient expression, we need to determine the second term in (A.3). For that, we multiply (4.9) by $\overline{L}(x,\mu)$ and (A.2) by $p_{\lambda_l}(x,\mu)$ and by integrating on X, we obtain

$$\begin{aligned} -\int_{-1}^{1}\int_0^D \mu\,\frac{\partial p_\lambda}{\partial x}(x,\mu,N)\overline{L}_\lambda(x,\mu,\overline{N})\, dxd\mu + \int_{-1}^{1}\int_0^D \sigma^\lambda_{ext}(N)\, p_\lambda(x,\mu,N)\overline{L}(x,\mu,\overline{N}) dxd\mu \\ = \int_{-1}^{1}\int_0^D \overline{L}_\lambda(x,\mu,\overline{N}) \int_{-1}^{1} p(x,\mu',N) f_\lambda(\mu',\mu,N) d\mu' dxd\mu \\ + \int_{-1}^{1}\int_0^D \overline{L}_\lambda(x,\mu,\overline{N}) \sum_{i=1}^{I} K(x_i,\lambda)\mathbb{1}_{(a,b)}(\mu)\,\delta_{x_i}(x)\, dx\, d\mu \end{aligned} \tag{A.4}$$

and

$$\begin{aligned} \int_{-1}^{1}\int_0^D \mu\, p_\lambda(x,\mu,N)\frac{\partial \overline{L}_\lambda}{\partial x}(x,\mu,\overline{N})\, dx\, d\mu + \int_{-1}^{1}\int_0^D \sigma_{ext}(\overline{N})\, p_\lambda(x,\mu,N)\, L_\lambda(x,\mu,N)\, dx\, d\mu \\ + \int_{-1}^{1}\int_0^D \sigma^\lambda_{ext}(N)\, p_\lambda(x,\mu,N)\, \overline{L}_\lambda(x,\mu,\overline{N})\, dx\, d\mu \\ = \int_{-1}^{1}\int_0^D p_\lambda(x,\mu,N) \int_{-1}^{1} L_\lambda(x,\mu',N) f_\lambda(\mu,\mu',\overline{N}) d\mu'\, dx\, d\mu \\ + \int_{-1}^{1}\int_0^D p_\lambda(x,\mu,N) \int_{-1}^{1} \overline{L}_\lambda(x,\mu',\overline{N}) f_\lambda(\mu,\mu',N) d\mu'\, dx\, d\mu \end{aligned} \tag{A.5}$$

by using the integration by part and that

$$\begin{aligned} \int_{-1}^{1}\int_0^D p_\lambda(x,\mu,N) \int_{-1}^{1} f_\lambda(\mu,\mu',N)\overline{L}_\lambda(x,\mu',\overline{N}) d\mu' dxd\mu = \\ \int_{-1}^{1}\int_0^D \overline{L}_\lambda(x,\mu,\overline{N}) \int_{-1}^{1} p(x,\mu',N) f_\lambda(\mu',\mu,N)\, d\mu' dxd\mu \end{aligned}$$

$$\int_{-1}^{1}\int_{0}^{D}\overline{L}_\lambda(x,\mu,\overline{N})\sum_{i=1}^{I}K(x_i,\lambda)\mathbb{1}_{(a,b)}(\mu)\,\delta_{x_i}(x)dxd\mu=\sum_{i=1}^{I}K(x_i,\lambda)\int_a^b\overline{L}_\lambda(x_i,\mu,\overline{N})d\mu$$

and by comparing (A.4) and (A.5), we obtain

$$\begin{aligned}\sum_{i=1}^{I}\sum_{l=1}^{G}K(x_i,\lambda_l)\int_a^b\overline{L}_{\lambda_l}(x_i,\mu,\overline{N})d\mu=&\sum_{l=1}^{G}\left[-\int_{-1}^{1}\int_0^D\sigma_{ext}^{\lambda_l}(\overline{N})p_{\lambda_l}(x,\mu,N)L_{\lambda_l}(x,\mu,N)dxd\mu\right]\\&+\sum_{l=1}^{G}\left[\int_{-1}^{1}\int_0^D p_{\lambda_l}(x,\mu,N)\int_{-1}^{1}L_{\lambda_l}(x,\mu',N)f_{\lambda_l}(\mu,\mu',\overline{N})d\mu'dxd\mu\right].\end{aligned}\tag{A.6}$$

Then, by (A.6) we obtain

$$\begin{aligned}DJ_\varepsilon(N)\cdot\overline{N}=&\,\varepsilon\int_0^{+\infty}r^2\,f(r)N\,\overline{N}\,dr-\sum_{l=1}^{G}\left[\int_{-1}^{1}\int_0^D p_{\lambda_l}(x,\mu,N)\,\sigma_{ext}^{\lambda_l}(\overline{N})\,L_{\lambda_l}(x,\mu,N)\,dx\,d\mu\right]\\&+\sum_{l=1}^{G}\left[\int_{-1}^{1}\int_0^D p_{\lambda_l}(x,\mu,N)\int_{-1}^{1}L_{\lambda_l}(x,\mu',N)\,f_{\lambda_l}(\mu,\mu',\overline{N})\,d\mu'\,dx\,d\mu\right].\end{aligned}\tag{A.7}$$

Appendix B. Computation of the decomposition of S_1 and S_2 on the basis of Legendre polynomial

To compute the decomposition (5.5) of S_1 and S_2 on the basis of Legendre polynomial, we express the polynomials π_n and τ_n occurring in (2.9)- (2.10) in function of the Legendre polynomials $(P_n)_{n\geq 0}$. We recall that

$$\pi_n(\mu)=P_n'(\mu),\qquad \tau_n(\mu)=-\mu\pi_n(\mu)+n(n+1)P_n(\mu),$$

in addition, by (5.1) and

$$\forall\, n\geq 2,\ P_n'(\mu)=P_{n-2}(\mu)-(2n-1)\,P_{n-1}'(\mu),\tag{B.1}$$

we obtain the following decomposition:

$$\pi_0=0,\ \text{ et }\forall n\geq 1,\pi_{2n}=\sum_{k=0}^{n-1}(4k+3)P_{2k+1},\pi_{2n-1}=\sum_{k=0}^{n-1}(4k+1)P_{2k},\tag{B.2}$$

$$\tau_0=0,\ \tau_1=P_1,\ \tau_{2n}=(2n)^2-\sum_{k=0}^{n-1}(4k+1)P_{2k},\ \tau_{2n-1}=(2n-1)^2-\sum_{k=0}^{n-2}(4k+3)P_{2k+1}.\tag{B.3}$$

By injecting (B.2),(B.3) in (2.9),(2.10), and (5.5), we obtain after some computations:

$$\forall k\geq 0,\begin{cases}\alpha_{2k}=\displaystyle\sum_{n=k\vee 2}^{+\infty}p_1(n,k)+\left(\frac{3}{2}a_1-\frac{5}{6}b_2\right)\delta_{k0}+\frac{10}{3}b_2\delta_{k1}\\[2ex]\alpha_{2k+1}=\displaystyle\sum_{n=(k+1)\vee 2}^{+\infty}i_1(n,k)+\left(\frac{3}{2}b_1+\frac{5}{2}a_2\right)\delta_{k0}\end{cases}$$

$$\forall k \geq 0, \begin{cases} \beta_{2k} = \displaystyle\sum_{n=k\vee 2}^{+\infty} p_2(n,k) + \left(\frac{3}{2}b_1 - \frac{5}{6}a_2\right)\delta_{k0} + \frac{10}{3}a_2\delta_{k1} \\ \\ \beta_{2k+1} = \displaystyle\sum_{n=(k+1)\vee 2}^{+\infty} i_2(n,k) + \left(\frac{3}{2}a_1 + \frac{5}{2}b_2\right)\delta_{k0} \end{cases}$$

with for $n \geq 2$:

$$\begin{cases} p_1(n,k) = -\dfrac{(4n+1)(4k+1)}{2n(2n+1)}b_{2n} + \dfrac{(4n-1)(4k+1)}{2n(2n-1)}a_{2n-1}, 0 \leq k \leq n-1 \\ \\ p_1(n,n) = \dfrac{4n+1}{2n(2n+1)}(2n)^2 b_{2n} \end{cases}$$

$$\begin{cases} i_1(n,k) = -\dfrac{(4n+1)(4k+3)}{2n(2n+1)}a_{2n} - \dfrac{(4n-1)(4k+3)}{2n(2n-1)}b_{2n-1}, 0 \leq k \leq n-2 \\ \\ i_1(n,n-1) = \dfrac{(4n+1)(4n-1)}{2n(2n+1)}a_{2n} + \dfrac{4n-1}{2n(2n-1)}(2n-1)^2 b_{2n-1} \end{cases}$$

$$\begin{cases} p_2(n,k) = -\dfrac{(4n+1)(4k+1)}{2n(2n+1)}a_{2n} + \dfrac{(4n-1)(4k+1)}{2n(2n-1)}b_{2n-1}, 0 \leq k \leq n-1 \\ \\ p_2(n,n) = \dfrac{4n+1}{2n(2n+1)}(2n)^2 a_{2n} \end{cases}$$

$$\begin{cases} i_2(n,k) = -\dfrac{(4n+1)(4k+3)}{2n(2n+1)}b_{2n} - \dfrac{(4n-1)(4k+3)}{2n(2n-1)}a_{2n-1}, 0 \leq k \leq n-2 \\ \\ i_2(n,n-1) = \dfrac{(4n+1)(4n-1)}{2n(2n+1)}b_{2n} + \dfrac{4n-1}{2n(2n-1)}(2n-1)^2 a_{2n-1}. \end{cases}$$

References

[1] Optical tomography using the time-independent equation of radiative transfer — part 1: forward model. *Journal of Quantitative Spectroscopy and Radiative Transfer*, 2002.

[2] United nations, economic and social council, economic commission for europe, new assessment/test method for automated driving (natm), 2021.

[3] European ccam partnership, strategic research and innovation agenda 2021-2027, v1.4, 2022.

[4] J.-C. Adams. *On the expression of the product of any two Legendre's coefficients by means of a series of Legendre's coefficients.* Proc. R. Soc. Lond G. Tschirhart, Caract´eristiques physiques g´en´erales des brouillards, Monographies de la, 1878.

[5] Ahmad Addoum, Olivier Farges, and Fatmir Asllanaj. Optical properties reconstruction using the adjoint method based on the radiative transfer equation. *Journal of Quantitative Spectroscopy and Radiative Transfer*, 204, 2018.

[6] Valeri Agoshkov and Valerij I Agoškov. *Boundary value problems for transport equations*. Springer Science & Business Media, 1998.

[7] G. Allaire and B.Despres F.Golse, X.Blanc. *Transport et diffusion*. CMAP, Ecole Polytechnique, 2019.

[8] Guillaume Bal and Alexandre Jollivet. Stability estimates in stationary inverse transport. *Inverse Problems and Imaging*, 2(4):427–454, 2008.

[9] Jonathan Barzilai and Jonathan Michael Borwein. Two-point step size gradient methods. *Ima Journal of Numerical Analysis*, 8:141–148, 1988.

[10] Kurt Beier and Hans Gemperlein. Simulation of infrared detection range at fog conditions for enhanced vision systems in civil aviation. *Aerospace Science and Technology*, 8(1):63–71, 2004. ISSN 1270-9638. doi: https://doi.org/10.1016/j.ast.2003.09.002. URL https://www.sciencedirect.com/science/article/pii/S1270963803000968.

[11] Thierry Bergot, Martial Haeffelin, Luc Musson-Genon, R. Tardiff, M. Colomb, Christophe Boitel, Guillaume Bouhours, T. Bourriane, Dominique Carrer, Jean Challet, Patrick Chazette, Philippe Drobinski, Éric Dupont, J.-C. Dupont, T. Elias, Clément Fesquet, Olivier Garrouste, L. Gomes, A. Guérin, Florian Lapouge, Y. Lefranc, D. Legain, P. Morange, Christophe Pietras, Artemio Plana-Fattori, Alain Protat, J. Rangognio, Jean-Christophe Raut, Samuel Rémy, David Richard, Balthasar E. de. Romand, and Xiuhui Zhang. Paris-fog : des chercheurs dans le brouillard. 2008.

[12] F Bernardin, M Colomb, F Egal, P Morange, and J Boreux. Droplet distribution models for visibility calculation. In *5th International Conference on Fog, Fog Collection and Dew*, number July, pages 2–5, Münster, 2010.

[13] Frédéric Bernardin, Roland Bremond, Vincent Ledoux, Maria Pinto, Sophie Lemonnier, Viola Cavallo, and Michèle Colomb. Measuring the effect of the rainfall on the windshield in terms of visual performance. *Accident Analysis and Prevention*, 63:83–88, 2014. ISSN 00014575. doi: 10.1016/j.aap.2013.10.008. URL http://dx.doi.org/10.1016/j.aap.2013.10.008.

[14] Mario Bijelic, Fahim Mannan, Tobias Gruber, Werner Ritter, Klaus Dietmayer, and Felix Heide. Seeing Through Fog Without Seeing Fog: Deep Sensor Fusion in the Absence of Labeled Training Data. *CoRR*, abs/1902.0, 2019. URL http://arxiv.org/abs/1902.08913.

[15] Bi Bo, Han Bo Han Weimin, Tang Jinping, and Li Li. Image reconstruction for diffuse optical tomography based on radiative transfer equation. *Computational and Mathematical Methods in Medicine*, 2015.

[16] Faisal S. Boudala, Di Wu, George A. Isaac, and Ismail Gultepe. Seasonal and microphysical characteristics of fog at a northern airport in alberta, canada. *Remote Sensing*, 14(19), 2022. ISSN 2072-4292. doi: 10.3390/rs14194865. URL https://www.mdpi.com/2072-4292/14/19/4865.

[17] K.M. Case and P.F. Zweifel. *Linear Transport Theory*. (Addison-Wesley, Reading, Massachusetts, 1967).

[18] Viola Cavallo, Michèle Colomb, and Jocelyne Doré. Distance Perception of Vehicle Rear Lights in Fog. *Human Factors*, 43(3):442–451, 2001. doi: 10.1518/001872001775898197. URL https://doi.org/10.1518/001872001775898197.

[19] Cerema. Adverse weather platform, available online: https://www.cerema.fr/en/innovation-recherche/innovation/offres-technologie/simulation-platform-adverse-climate-conditions.

[20] S. Chandrasekhar. *Radiative Transfer*. Dover, New York, 1960.

[21] M Choulli and P Stefanov. Reconstruction of the coefficients of the stationary transport equation from boundary measurements. *Inverse Problems*, 12(5):L19–L23, oct 1996. doi: 10.1088/0266-5611/12/5/001.

[22] M Colomb, F Bernardin, and P Morange. Paramétrisation de la visibilité et modelisation de la distribution granulométrique à partir de données microphysiques. In *Séminaire AMA 2008 Météo France*, pages 1–10, 2008.

[23] M. Colomb, K. Hirech, P. André, J.J. Boreux, P. Lacôte, and J. Dufour. An innovative artificial fog production device improved in the European project "FOG". *Atmospheric Research*, 87 (3-4):242–251, mar 2008. ISSN 01698095. doi: 10.1016/j.atmosres.2007.11.021. URL http://linkinghub.elsevier.com/retrieve/pii/S0169809507002037.

[24] Khouloud Dahmane, Pierre Duthon, Frédéric Bernardin, Michèle Colomb, Najoua Essoukri Ben Amara, and Frédéric Chausse. The Cerema pedestrian database : A specific database in adverse weather conditions to evaluate computer vision pedestrian detectors. In *7th Conference on Sciences of Electronics, Technologies of Information and Telecommunications (SETIT)*, pages 480–485, 2016.

[25] Khouloud Dahmane, Pierre Duthon, Frédéric Bernardin, Michèle Colomb, Frédéric Chausse, and Christophe Blanc. Weathereye-proposal of an algorithm able to classify weather conditions from traffic camera images. *Atmosphere*, 12(6), 2021. ISSN 2073-4433. doi: 10.3390/atmos12060717. URL https://www.mdpi.com/2073-4433/12/6/717.

[26] D. Deirmendjian. Electromagnetic Scattering on Spherical Polydispersions, 1969. ISSN 1477870X.

[27] Diran Deirmendjian. *Electromagnetic Scattering on Spherical Polydispersions*. RAND Corporation, Santa Monica, CA, 1969.

[28] Pierre Duthon, Frédéric Bernardin, Frédéric Chausse, and Michèle Colomb. Methodology used to evaluate computer vision algorithms in adverse weather conditions. In *Proceedings of 6th Transport Research Arena*, Warsaw, Poland, 2016.

[29] Pierre Duthon, Michèle Colomb, and Frédéric Bernardin. Light Transmission in Fog: The Influence of Wavelength on the Extinction Coefficient. *Applied Sciences*, 9(14):2843, 2019. ISSN 2076-3417. doi: 10.3390/app9142843.

[30] Pierre Duthon, Michèle Colomb, and Frédéric Bernardin. Fog classification by their droplet size distributions: Application to the characterization of cerema's platform. *Atmosphere*, 11 (6), 2020. ISSN 2073-4433. doi: 10.3390/atmos11060596. URL https://www.mdpi.com/2073-4433/11/6/596.

[31] Herbert Egger and Matthias Schlottbom. Numerical methods for parameter identification in stationary radiative transfer jo - computational optimization and applications. *Journal of Mathematical Physics*, 2015.

[32] T. Elias, J. C. Dupont, E. Hammer, C. R. Hoyle, M. Haeffelin, F. Burnet, and D. Jolivet. Enhanced extinction of visible radiation due to hydrated aerosols in mist and fog. *Atmospheric Chemistry and Physics*, 15(12):6605–6623, 2015. ISSN 16807324. doi: 10.5194/acp-15-6605-2015.

[33] Jamil Fayyad, Mohammad A. Jaradat, Dominique Gruyer, and Homayoun Najjaran. Deep learning sensor fusion for autonomous vehicle perception and localization: A review. *Sensors*, 20(15), 2020. ISSN 1424-8220. doi: 10.3390/s20154220. URL https://www.mdpi.com/1424-8220/20/15/4220.

[34] T Feng, P Edström, and M Gulliksson. Levenberg–marquardt methods for parameter estimation problems in the radiative transfer equation. *Inverse Problems*, mar 2007.

[35] Bruce W. Fowler. Expansion of mie-theory phase functions in series of legendre polynomials. *J. Opt. Soc. Am.*, 73(1):19–22, Jan 1983.

[36] Sandro Fuzzi, Mario Gazzi, Cesare Pesci, and Vittorio Vicentini. A linear impactor for fog droplet sampling. *Atmospheric Environment (1967)*, 14(7):797–801, 1980. ISSN 00046981. doi: 10.1016/0004-6981(80)90135-3.

[37] F. García-García, U Virafuentes, and G. Montero-Martínez. Fine-scale measurements of fog-droplet concentrations: A preliminary assessment. *Atmospheric Research*, 64(1-4):179–189, 2002. ISSN 01698095. doi: 10.1016/S0169-8095(02)00090-X.

[38] J A Garland. Some fog droplet size distributions obtained by an impaction method. *Quarterly Journal of the Royal Meteorological Society*, 97(414):483–494, 1971. ISSN 1477870X. doi: 10.1002/qj.49709741408.

[39] H. E. Gerber. Microstructure of a radiation fog. *Journal of the Atmospheric Sciences*, 38(2): 454–458, 1981. ISSN 00224928. doi: 10.1175/1520-0469(1981)038⟨0454:MOARF⟩2.0.CO;2.

[40] Jindra Goodman. The Microstructure of California Coastal Fog and Stratus. *Journal of Applied Meteorology*, 16(10):1056–1067, 1977. ISSN 0021-8952. doi: 10.1175/1520-0450(1977)016⟨1056:tmoccf⟩2.0.co;2.

[41] Martin Grabner and Vaclav Kvicera. The wavelength dependent model of extinction in fog and haze for free space optical communication. *Opt. Express*, 19(4):3379–3386, Feb 2011. doi: 10.1364/OE.19.003379. URL https://opg.optica.org/oe/abstract.cfm?URI=oe-19-4-3379.

[42] Jinlan Guan, Shaomei Fang, and Changhong Guo. Optical tomography reconstruction algorithm based on the radiative transfer equation considering refractive index: Part 2. inverse model. *Computerized Medical Imaging and Graphics*, 2013.

[43] Ismail Gultepe, R. Tardif, Silas C. Michaelides, J. Cermak, A. Bott, J. Bendix, M. D. Müller, Mariusz Pagowski, B. Hansen, Gary Ellrod, Wilfried Jacobs, Garrym Toth, and Stewart G. Cober. Fog research: A review of past achievements and future perspectives. *Pure and Applied Geophysics*, 2007. ISSN 00334553. doi: 10.1007/s00024-007-0211-x.

[44] Ismail Gultepe, Jason A. Milbrandt, and Binbin Zhou. *Marine Fog: A Review on Microphysics and Visibility Prediction*, pages 345–394. Springer International Publishing, Cham, 2017. ISBN 978-3-319-45229-6. doi: 10.1007/978-3-319-45229-6_7. URL https://doi.org/10.1007/978-3-319-45229-6_7.

[45] M. Haeffelin, T. Bergot, T. Elias, R. Tardif, D. Carrer, P. Chazette, M. Colomb, P. Drobinski, E. Dupont, J.-C. Dupont, L. Gomes, L. Musson-Genon, C. Pietras, Artemio Plana-Fattori, Alain Protat, J. Rangognio, Jean-Christophe Raut, S. Rémy, D. Richard, J. Sciare, and X. Zhang. PARISFOG: Shedding New Light on Fog Physical Processes. *Bulletin of the American Meteorological Society*, 91:767–783, 2010. doi: 10.1175/2009BAMS2671.1. URL https://hal.science/hal-00497276.

[46] William W. Hager and Hongchao Zhang. A survey of nonlinear conjugate gradient methods. 2005.

[47] Jianxin He, Xinyue Ren, Hao Wang, Zhao Shi, Fugui Zhang, Lijun Hu, Qiangyu Zeng, and Xin Jin. Analysis of the microphysical structure and evolution characteristics of a typical sea fog weather event in the eastern sea of china. *Remote Sensing*, 14(21), 2022. ISSN 2072-4292. doi: 10.3390/rs14215604. URL https://www.mdpi.com/2072-4292/14/21/5604.

[48] Zhenzong He, Hong Qi, Yuchen Yao, and Liming Ruan. Inverse estimation of the particle size distribution using the fruit fly optimization algorithm. *Applied Thermal Engineering*, 88: 306–314, 2015. ISSN 1359-4311. Special Issue for International Heat Transfer Symposium 2014.

[49] Zhenzong He, Hong Qi, Zhongyuan Lew, Liming Ruan, Heping Tan, and Kun Luo. Application of the lsqr algorithm in non-parametric estimation of aerosol size distribution. *Optics Communications*, 2016.

[50] J. Allen Zak. Drop Size Distributions and Related Properties of Fog for Five. Technical Report April 1994, NASA, 1994.

[51] Alexander D. Klose and Andreas H. Hielscher. Optical tomography using the time-independent equation of radiative transfer—part 2: inverse model. *Journal of Quantitative Spectroscopy and Radiative Transfer*, 2002.

[52] Motoi Kumai. Arctic Fog Droplet Size Distribution and Its Effect on Light Attenuation. *Journal of the Atmospheric Sciences*, 30(4):635–643, 1973. ISSN 0022-4928. doi: 10.1175/1520-0469(1973)030⟨0635:afdsda⟩2.0.co;2.

[53] Bruce A. Kunkel. Fog Drop-Size Distributions Measured with a Laser Hologram Camera. *Journal of Applied Meteorology*, 10(3):482–486, 1971. ISSN 0021-8952. doi: 10.1175/1520-0450(1971)010⟨0482:fdsdmw⟩2.0.co;2.

[54] Bruce A. Kunkel. Comparison of Fog Drop Size Spectra Measured by Light Scattering and Impaction Techniques. Technical report, Air Force Geophysics Laboratory, Air Force Systems Command, United States Air Force, 1981.

[55] Bruce A. Kunkel. Microphysical Properties of Fog at Otis AFB. Technical report, Air Force Geophysics Laboratory, Air Force Systems Command, United States Air Force, 1982.

[56] Bruce A Kunkel. Parameterization of droplet terminal velocity and extinction coefficient in fog models. *Journal of Climate and applied meteorology*, 23(1):34–41, 1984.

[57] Matti Kutila, Pasi Pyykönen, H. Holzhuter, Michèle Colomb, and Pierre Duthon. Automotive lidar performance verification in fog and rain. *2018 21st International Conference on Intelligent Transportation Systems (ITSC)*, 2018.

[58] René Lagrange. *Polynômes et fonctions de Legendre*. Mémorial des sciences mathématiques. Gauthier-Villars, 1939.

[59] Frank Lenzen and Otmar Scherzer. Tikhonov type regularization methods: History and recent progress. *Proceeding Eccomas*, 2004, 01 2004.

[60] Kenneth Levenberg. A method for the solution of certain non – linear problems in least squares. *Quarterly of Applied Mathematics*, 2:164–168, 1944.

[61] J. Li, C. Zhu, H. Chen, D. Zhao, L. Xue, X. Wang, H. Li, P. Liu, J. Liu, C. Zhang, Y. Mu, W. Zhang, L. Zhang, H. Herrmann, K. Li, M. Liu, and J. Chen. The evolution of cloud and aerosol microphysics at the summit of mt. tai, china. *Atmospheric Chemistry and Physics*, 20 (22):13735–13751, 2020. doi: 10.5194/acp-20-13735-2020. URL https://acp.copernicus.org/articles/20/13735/2020/.

[62] You Li, Pierre Duthon, Michèle Colomb, and Javier Ibanez-Guzman. What happens for a tof lidar in fog? *IEEE Transactions on Intelligent Transportation Systems*, 2021.

[63] Qing Liu, Bingui Wu, Zhaoyu Wang, and Tianyi Hao. Fog droplet size distribution and the interaction between fog droplets and fine particles during dense fog in tianjin, china. *Atmosphere*, 11(3), 2020. ISSN 2073-4433. doi: 10.3390/atmos11030258. URL https://www.mdpi.com/2073-4433/11/3/258.

[64] J. V. Mallow. Empirical fog droplet size distribution functions with finite limits. *Journal of the atmospheric sciences*, 32(2 (February, 1975)):440–443, 1975. ISSN 0022-4928. doi: 10.1175/1520-0469(1975)032⟨0440:efdsdf⟩2.0.co;2.

[65] Mario Marchetti, Vincent Boucher, Jean Dumoulin, and Michèle Colomb. Retrieving visibility distance in fog combining infrared thermography, Principal Components Analysis and Partial Least-Square regression. *Infrared Physics and Technology*, 71:289–297, 2015. ISSN 13504495. doi: 10.1016/j.infrared.2015.05.002. URL http://dx.doi.org/10.1016/j.infrared.2015.05.002.

[66] M. Mazoyer, F. Burnet, and C. Denjean. Experimental study on the evolution of droplet size distribution during the fog life cycle. *Atmospheric Chemistry and Physics*, 22(17):11305–11321, 2022. doi: 10.5194/acp-22-11305-2022. URL https://acp.copernicus.org/articles/22/11305/2022/.

[67] N. J. McCormick. Methods for solving inverse problems for radiation transport—an update. *Transport Theory and Statistical Physics*, 1986.

[68] N. J. McCormick. Inverse radiative transfer problems: A review. *Nuclear Science and Engineering*, 1992.

[69] M. B. Meyer, J. E. Jiusto, and G. G. Lala. Measurements of visual range and radiation-fog (haze) microphysics. *Journal of the Atmospheric Sciences*, 37(3):622–629, 1980. ISSN 00224928. doi: 10.1175/1520-0469(1980)037⟨0622:MOVRAR⟩2.0.CO;2.

[70] Răzvan-Cătălin Miclea, Vlad-Ilie Ungureanu, Florin-Daniel Sandru, and Ioan Silea. Visibility enhancement and fog detection: Solutions presented in recent scientific papers with potential for application to mobile systems. *Sensors*, 21(10), 2021. ISSN 1424-8220. doi: 10.3390/s21103370. URL https://www.mdpi.com/1424-8220/21/10/3370.

[71] Abdul Sajeed Mohammed, Ali Amamou, Follivi Kloutse Ayevide, Sousso Kelouwani, Kodjo Agbossou, and Nadjet Zioui. The perception system of intelligent ground vehicles in all weather conditions: A systematic literature review. *Sensors*, 20(22), 2020. ISSN 1424-8220. doi: 10.3390/s20226532. URL https://www.mdpi.com/1424-8220/20/22/6532.

[72] Frederic Paletou. Une introduction au transfert de rayonnement astrophysique. April 2020.

[73] Nicolas Pinchon, Olivier Cassignol, A Nicolas, Patrick Leduc, Jean Philippe Tarel, Roland Bremond, G Julien, Nicolas Pinchon, Olivier Cassignol, A Nicolas, Frédéric Bernardin, N Pinchon, O Cassignol, A Nicolas, F Bernardin, P Leduc, and J-p Tarel. All-weather vision for automotive safety : which spectral band ? In *SIA Vision 2016 - International Conference Night Drive Tests and Exhibition*, 2016.

[74] R. G. Pinnick, D. L. Hoihjelle, G. Fernandez, E. B. Stenmark, J. D. Lindberg, G. B. Hoidale, and S. G. Jennings. Vertical Structure in Atmospheric Fog and Haze and Its Effects on Visible and Infrared Extinction. *Journal of the Atmospheric Sciences*, 35(10):2020–2032, 1978. ISSN 0022-4928. doi: 10.1175/1520-0469(1978)035⟨2020:vsiafa⟩2.0.co;2.

[75] J. D. Price, S. Lane, I. A. Boutle, D. K. E. Smith, T. Bergot, C. Lac, L. Duconge, J. McGregor, A. Kerr-Munslow, M. Pickering, and R. Clark. Lanfex: A field and modeling study to improve our understanding and forecasting of radiation fog. *Bulletin of the American Meteorological Society*, 99(10):2061 – 2077, 2018. doi: 10.1175/BAMS-D-16-0299.1. URL https://journals.ametsoc.org/view/journals/bams/99/10/bams-d-16-0299.1.xml.

[76] Jeremy Price. Radiation Fog. Part I: Observations of Stability and Drop Size Distributions. *Boundary-Layer Meteorology*, 139(2):167–191, May 2011. doi: 10.1007/s10546-010-9580-2.

[77] European project ROADVIEW. European project roadview, available online: https:// https://roadview-project.eu/.

[78] Yaobin Qiao, Hong Qi, Qin Chen, Liming Ruan, and Heping Tan. An efficient and robust reconstruction method for optical tomography with the time-domain radiative transfer equation. *Optics and Lasers in Engineering*, 2016.

[79] Boris Quétard, Jean-Charles Quinton, Michele Colomb, Giovanni Pezzulo, Laura Barca, Marie Izaute, Owen Kevin Appadoo, and Martial Mermillod. Combined effects of expectations and visual uncertainty upon detection and identification of a target in the fog. *Cognitive processing*, 16(1):343–348, 2015.

[80] Jacques-Louis Lions Robert Dautray. *Mathematical Analysis and Numerical Methods for Science and Technology: Volume 6 Evolution Problems II*. Springer Berlin Heidelberg, Berlin, Heidelberg, 2000.

[81] Francisca Rosique, Pedro J. Navarro, Carlos Fernández, and Antonio Padilla. A systematic review of perception system and simulators for autonomous vehicles research. *Sensors*, 19(3), 2019. ISSN 1424-8220. doi: 10.3390/s19030648. URL https://www.mdpi.com/1424-8220/19/3/648.

[82] David J. Segelstein. *The Complex Refractive Index of Water*. Theses, M.S. Thesis, University of Missouri–Kansas City, 1981.

[83] Eric P. Shettle and Robert W Fenn. Models for the aerosols of the lower atmosphere and the effects of humidity variations on their optical properties. *Environmental Research Paperr*, 676 (6):89, 1979. ISSN 0018-9529. doi: 10.1109/TR.1987.5222381.

[84] Eric P. Shettle and Robert W. Fenn. Models for the aerosols of the lower atmosphere and the effects of humidity variations on their optical properties. 1979.

[85] Dorathy A. Stewart and Oskar M. Essenwanger. A survey of fog and related optical propagation characteristics, 1982. ISSN 19449208.

[86] Xiaogang Sun, Hong Tang, and Guibin Yuan. Anomalous diffraction approximation method for retrieval of spherical and spheroidal particle size distributions in total light scattering. *Journal of Quantitative Spectroscopy and Radiative Transfer*, 2008.

[87] Xiaogang Sun, Hong Tang, and Jingmin Dai. Inversion of particle size distribution from spectral extinction data using the modified beta function. *Powder Technology*, 190(3), 2009.

[88] Francesco Tampieri and Claudio Tomasi. Size distribution models of fog and cloud droplets in terms of the modified gamma function. *Tellus*, 28(4):333–347, 1976. ISSN 0040-2826. doi: 10.3402/tellusa.v28i4.10300.

[89] Boris Thies, Sebastian Egli, and Jörg Bendix. The influence of drop size distributions on the relationship between liquid water content and radar reflectivity in radiation fogs. *Atmosphere*, 8(8), 2017. ISSN 20734433. doi: 10.3390/atmos8080142.

[90] Jorge Vargas, Suleiman Alsweiss, Onur Toker, Rahul Razdan, and Joshua Santos. An overview of autonomous vehicles sensors and their vulnerability to weather conditions. *Sensors*, 21(16), 2021. ISSN 1424-8220. doi: 10.3390/s21165397. URL https://www.mdpi.com/1424-8220/21/16/5397.

[91] Curtis L. Walker, Brenda Boyce, Christopher P. Albrecht, and Amanda Siems-Anderson. Will weather dampen self-driving vehicles? *Bulletin of the American Meteorological Society*, 101(11):E1914 – E1923, 2020. doi: 10.1175/BAMS-D-19-0035.1. URL https://journals.ametsoc.org/view/journals/bams/101/11/bamsD190035.xml.

[92] W. J. Wiscombe. *Improved mie scattering algorithms*. Appl. Opt., 19, 1980.

[93] World Meteorological Organization (WMO). *Guide to Instruments and Methods of Observation*. (WMO-No. 8), 2018 (first edition published in 1950).

[94] Yuan Yuan, Hong-Liang Yi, Yong Shuai, Fu-Qiang Wang, and He-Ping Tan. Inverse problem for particle size distributions of atmospheric aerosols using stochastic particle swarm optimization. *Journal of Quantitative Spectroscopy and Radiative Transfer*, 2010.

[95] J. Yvon. La diffusion macroscopique des neutrons une methode d'approximation. *Journal of Nuclear Energy (1954)*, 1957.